Mechanics of Three-Dimensional Micro-Architected Interpenetrating Phase Composites

by

Andrew Y. Chen

B.S. Mechanical Engineering, University of California, Berkeley, 2022

Submitted to the Department of Mechanical Engineering
in partial fulfillment of the requirements for the degree of

MASTER OF SCIENCE IN MECHANICAL ENGINEERING

at the

MASSACHUSETTS INSTITUTE OF TECHNOLOGY

September 2024

Authored by: Andrew Y. Chen
Department of Mechanical Engineering
August 9, 2024

Certified by: Carlos M. Portela
Robert N. Noyce Career Development Assistant Professor, Mechanical Engineering
Thesis Supervisor

Accepted by: Nicolas Hadjiconstantinou
Professor of Mechanical Engineering
Chair, Department of Mechanical Engineering Committee on Graduate Students

Mechanics of Three-Dimensional Micro-Architected Interpenetrating Phase Composites

by

Andrew Y. Chen

Submitted to the Department of Mechanical Engineering
on August 9, 2024 in partial fulfillment of the requirements for the degree of

MASTER OF SCIENCE IN MECHANICAL ENGINEERING

ABSTRACT

The design of modern composite materials, as used in a wide range of engineering applications, is largely derived from a traditional framework based on laminates. While resulting in desirable strength and stiffness properties, the laminate-based structure leads to a high degree of anisotropy and unique failure modalities like interlaminar failure, limiting the performance of these composites under complex loading conditions. Meanwhile, recent work in the field of architected materials has yielded a thorough understanding of geometry-dependent material behavior, enabling the development of highly robust architectures with tunable (an)isotropy. However, such advances have focused primarily on describing the response of lightweight architected geometries comprised mostly of air. The effect of adding a load-bearing matrix is not well understood.

Here we investigate the effect of geometry and constituent material properties on the mechanics of 3D-architected interpenetrating phase composite (IPC) materials, i.e., two-phase materials consisting of an architected structure surrounded by a matrix. Using computational homogenization, we first predict how resultant coupled stress states in the composite change with the material properties of each individual phase and contextualize the results within traditional stiffness scaling laws. We then demonstrate two robust fabrication pathways for realizing polymer- and carbon-based centimeter-scale architected IPCs with micro-scale features. Using these prototypes, we study the mechanical behavior of the fabricated composites under uniaxial compression, with particular emphasis on the non-linear and failure regimes. We show that independent of the material system, the presence of a load-bearing matrix distributes the stress in the composite, contributing to a high-strength, globally stretching-dominated failure behavior, regardless of nodal connectivity. Moreover, the development of a 3D, highly tortuous pathway for stress delays or prevents catastrophic failure of the traditionally brittle architecture phase, resulting in energy dissipation performance of the composite that exceeds the sum of its individual constituents.

Finally, we demonstrate that the composite stress state can be architected using geometric design of the IPC and introduce an example of tunable mechanical response in an architected composite inspired by traditional auxetic metamaterials. Altogether, this work broadens our established understanding of the link between architecture and mechanical performance by considering the framework of interpenetrating phase composites, creating the foundation for a new class of strong, resilient, and programmable materials with architected stress states.

Thesis supervisor: Carlos M. Portela
Title: Robert N. Noyce Career Development Assistant Professor, Mechanical Engineering

Acknowledgments

First, I would like to thank my advisor and mentor, Professor Carlos Portela, who has been an invaluable source of support, guidance, and inspiration during my time as a Master's student. Carlos, your unwavering commitment has increased my confidence and furthered my enthusiasm for practicing and communicating science. I am grateful for the opportunity to work with you, and I am excited to keep exploring the vast realm of architected materials with you at the helm.

I would also like to extend my appreciation towards several professors I have had the privilege of learning from. Professor Rohan Abeyaratne, thank you for your mentorship and support during these first years in graduate school. Professor Ken Kamrin, your enthusiasm for mechanics and your passion for teaching is infectious and inspirational. Professor Lallit Anand, I am grateful for your expertise and for providing a thorough foundation in solid mechanics, one on which I hope to build during the rest of my time in graduate school.

I am grateful to the members of the Portela Research Group — James Surjadi, Molly Carton, Jet Lem, Somayajulu Dhulipala, Thomas Butruille, Rachel Sun, Michael Espinal, Samuel Figueroa, Rishi Kommalapati, and Carlo Pignagnoli — for being excellent colleagues, teammates, and friends. Your drive and your talent motivates me every day. In particular, I would like to thank James, Rachel, Somayajulu, Rishi, and Jet for sharing their insightful and valuable advice, feedback, and experience. I would also like to extend heartfelt appreciation to my undergraduate assistant, Collin DesRoberts, for his assistance with fabrication and characterization. This work would not have been possible without all of your contributions.

To my friends Lale, Aaditya, Theo, and Chris, thank you for your companionship, support, and humor, especially when things were toughest. You all have made my time at MIT incredibly enjoyable.

Finally, I have been incredibly fortunate to have the enduring support of my wonderful family: my sister Lauren, my parents Peter and Teresa, and my girlfriend Laura. I am grateful for your sacrifices, love, and encouragement, which have made me the person I am today. I hope that I can make you proud.

Contents

List of Figures

List of Tables

Chapter 1

Introduction

1.1 Architected materials

Nature has endowed us with a broad range of materials, spanning properties from lightweight to dense, compliant to stiff, and weak to strong. Over millenia, humans have further expanded the property space of natural materials, creating new materials and finding new ways to make them. Ashby [1] first illustrated the landscape of this property space using the eponymous "Ashby chart" of stiffness and density, as shown in Figure 1.1. Similar plots exist for strength, toughness, electrical conductivity, and a number of other physical properties of materials; these charts have become ubiquitous design tools across engineering.

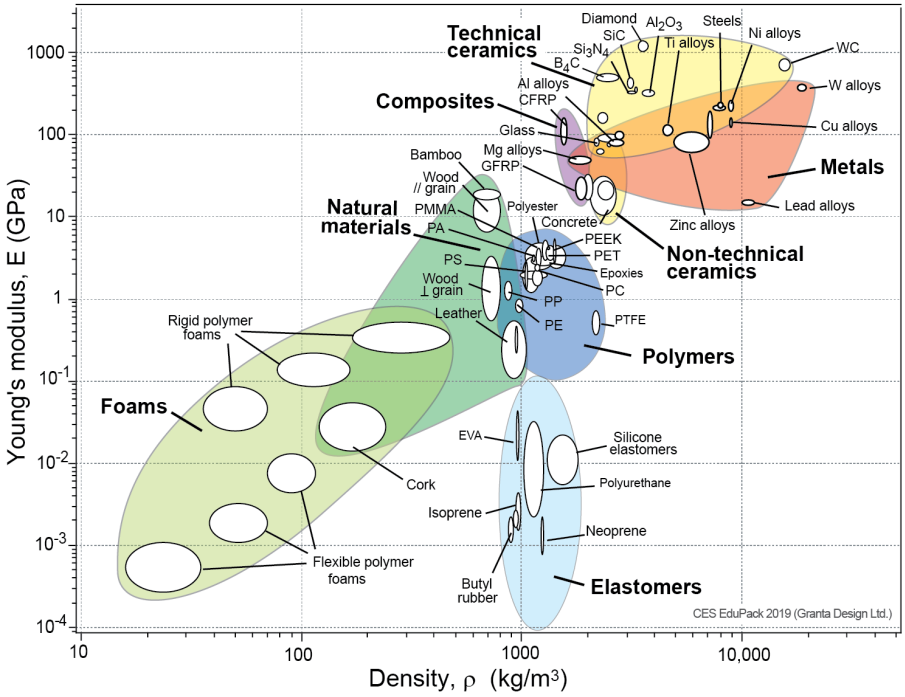

Figure 1.1: Ashby chart of Young's modulus versus density. Chart created using CES EduPack 2019, ANSYS Granta © 2020 Granta Design.

The Ashby plot for stiffness and density (Figure 1.1) tells a compelling story not only in the shaded material regimes, but also in the whitespace left behind. It reveals that a tradeoff exists between stiffness and density; in particular, no monolithic material, natural or man-made, has simultaneously attained low density and high stiffness. This was one original motivation for the field of *architected materials*, which has since evolved toward the broader goal of engineering particular material properties not before seen in "traditional" materials. Typically, a combination of morphology — the architecture — and the underlying material (polymer, metal, etc.) is used to achieve a behavior of interest. Over the last few decades, architected materials (also called mechanical metamaterials) have demonstrated a variety of outstanding material responses [2], including the achievement of specific stiffness near the theoretical limit [3]. Today, architected materials continue to be studied not only for their mechanical properties [4], but also for multifunctional applications [5, 6], both of which depend on and take advantage of a high degree of tunability afforded by the architectural design.

Of particular interest are architected materials having features at the microscale and below. It has been shown that downscaling takes advantage of certain "size effects", by which remarkable improvements in mechanical properties (e.g., strengthening, toughening, or the suppression of failure mechanisms) are attained by a reduction in the feature size [7, 8]. Moreover, the advent of additive manufacturing technologies with sub-micron resolution, like two-photon lithography (TPL), and the subsequent emergence of commercial TPL systems, has made the realization of microscale architected materials possible [9]. Such materials can achieve a *separation of scales*, whereby the characteristic length scale associated with geometric features (e.g., the diameter of an individual beam) is entirely separate from the (larger) characteristic length scale associated with the specimen. Importantly, only when an adequate separation of scales is achieved can a true *material* response be measured, and the properties of an architected *material* be validated.

1.2 Bending and stretching

A fundamental classification metric for beam-based architected materials is their response to infinitesimal deformation, such as an infinitesimal uniaxial compression [10, 11, 12]. In this elastic limit, unit cells, assumed to be made up of slender (i.e., high-aspect-ratio) cylindrical beams, are classified as either bending-dominated or stretching-dominated. A bending-dominated material is one whose beams (of length L, area moment of inertia I, and Young's modulus E) follow the force-displacement relation

$$\delta = \frac{C_1 P L^3}{EI}, \tag{1.1}$$

where δ is the displacement, P is the force, and C_1 is a constant. Conversely, a stretching-dominated material has beams for which

$$\delta = \frac{C_2 P L}{AE} \tag{1.2}$$

holds; here, A is the cross-sectional area and C_2 is another proportionality constant. Furthermore, it can be shown that for cylindrical beam-based architectures, to leading order,

the *relative density* (or volume fill fraction) $\tilde{\rho}$ scales quadratically with the aspect ratio r/L; that is,

$$\tilde{\rho} = C_3(r/L)^2 \tag{1.3}$$

for C_3 a constant. For such a structure, the second area moment I scales with the fourth power of the characteristic beam radius r, and the cross-sectional area of a beam scales quadratically with r.

Now, given a far-field applied uniaxial stress $\sigma \propto P/L^2$ on a unit cell, let the corresponding uniaxial strain be $\varepsilon \propto \delta/L$. The ratio of these is defined to be the *effective stiffness* E' of the unit cell in the direction of loading. Let $\tilde{E} \equiv E'/E$ represent the *relative stiffness* of the material, which is the ratio of the effective stiffness to the Young's modulus of the constituent material. By combining (1.3) with (1.1) and (1.2), it can be shown that the relative stiffness and relative density are related by

$$\tilde{E} = C\tilde{\rho}^m, \tag{1.4}$$

where C is a constant, $m = 2$ for a bending-dominated structure, and $m = 1$ for a stretching-dominated structure [13].

For a beam-based unit cell, it can be shown that a necessary, but not sufficient, condition for a stretching-dominated response is the fulfillment of *Maxwell's criterion*, which for a three-dimensional architecture reads

$$b - 3j + 6 \geq 0 \tag{1.5}$$

where b is the number of beams and j the number of nodes [10, 14]. (A necessary *and* sufficient condition requires that the structure admit no zero-energy mechanisms if pin-jointed.) Therefore, a structure not satisfying Maxwell's criterion must be bending-dominated. One such example is the Kelvin cell (or regular tetrakaidecahedron), which consists of six quadrilateral and eight hexagonal faces [15]. The Kelvin cell has been well studied in the architected materials literature as a classical example of a bending-dominated structure [16, 17].

Importantly, it must be emphasized that the "classical" scaling-law results apply only in the limit for which (1.1) and (1.2) hold; namely, in the *high-slenderness* limit, $r/L \to 0$, typically corresponding to the low relative density limit $\tilde{\rho} \to 0$. Moreover, this theoretical analysis ignores the effect of local bending moments carried by real solid-joined nodes. Due to the geometry of the as-fabricated nodal joints between beams, as well as the finite slenderness of most fabricated architected materials, the scaling exponent of real architected materials lies somewhere between 1 and 2 for stretching-dominated structures, and typically above 2 for bending-dominated structures [16, 18, 19].

Nevertheless, several remarkable examples of architected materials have obtained near-ideal scaling behavior, or in other words a stiffness-to-weight ratio approaching the theoretical limit. These materials typically achieve truly stretching-dominated responses either by the use of geometries other than beams (e.g., plates or shells [20, 21, 22, 23]) or by taking advantage of scale effects (e.g., having feature sizes at the nanoscale [24, 3]). As these examples demonstrate, the pursuit of a structurally-efficient stretching-dominated response remains an active research interest in the field.

1.3 Composite materials across length scales

Meanwhile, composite materials have come to be used in a wide range of important engineering applications across disciplines. Among other desirable properties, composites possess a high specific stiffness, as shown on the Ashby plot of Figure 1.1. For this reason, such composites have become ubiquitous across aerospace, automotive, and military applications, among others. Although composite materials are found in many forms, the fundamental concept underlying their robust mechanical performance is *load transfer* [25], whereby an applied load is distributed among the distinct material phases.

The most common type of composite material use in engineering applications consists of *laminates*, which is a stack of *laminae* (a lamina is also called a *ply*), each of which are in turn made up of oriented fibers embedded in a matrix material (Figure 1.2(a-b)). Despite the benefits offered by a two-phase system, the inherent oriented nature of the fibers within a lamina results in a high degree of anisotropy: the lamina is much stronger and stiffer when loaded in a direction parallel to the fibers compared to any other direction. Even when multiple plies are stacked in a laminate structure, significant anisotropy remains [26]. Moreover, the layer-wise nature of the laminate structure results in the possibility of failure by *delamination*, whereby individual laminae remain intact, but successive plies debond from each other. Failure by delamination is typically catastrophic, and usually occurs at applied stress levels lower than the ideal failure strength of the laminate, because the interlayer bonding is often much weaker than the in-plane strength of the fibers and because there are few mechanisms by which energy may be absorbed in this type of failure [27, 28]. For these reasons, delamination is an important and dangerous failure mode for consideration in the design of composite materials (Figure 1.2(c)).

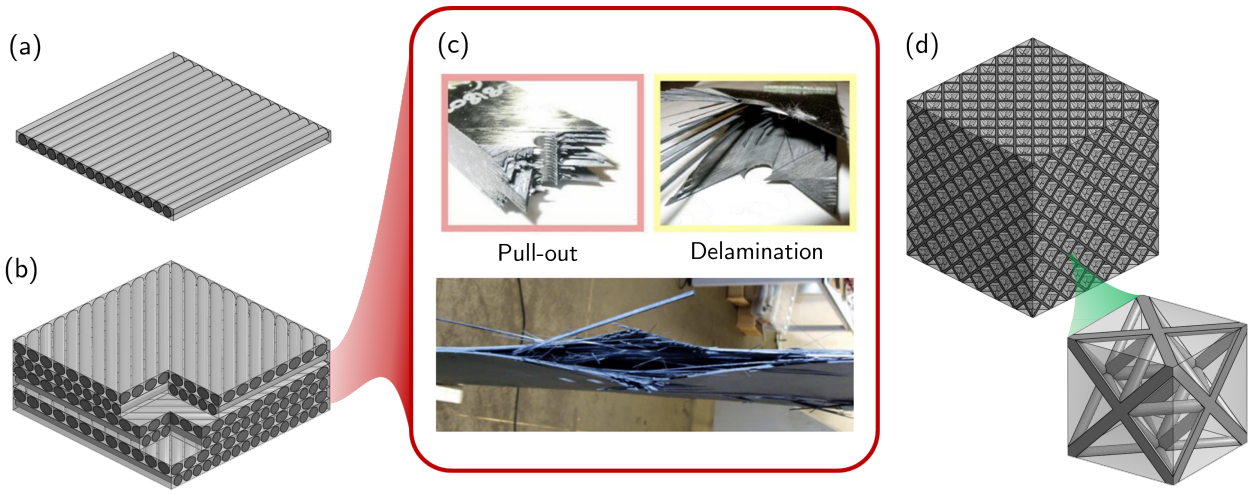

Figure 1.2: Structure of composite materials: in a laminated composite, individual laminae (a), consisting of oriented fibers within a matrix, are stacked to create a laminate (b). Laminated composites can fail catastrophically by fiber pull-out or by delamination (c); reproduced from [27]. In contrast, an interpenetrating phase composite (d) has two distinct, self-supporting material networks spanning all spatial dimensions.

However, delamination is a failure mode caused by the two-dimensional character of

laminated composites, and therefore unique to this type of structure. One type of composite structure that has been of recent research interest is the three-dimensional *interpenetrating phase composite* (IPC, Figure 1.2(d)), which consists of distinct material networks, each continuously interconnected and self-supported throughout the entire length of a material sample [29]. In particular, IPCs which contain structural features in three dimensions are naturally robust against failure by delamination, due to the lack of individual laminae in their structure. Indeed, IPCs have been shown to demonstrate an improved tolerance to loading from an arbitrary orientation, as well as inherently high strength and resistance to fracture [30, 31, 32]. In this work, we aim to unify the frameworks of micro-scale architected materials and composite materials to create three-dimensional *micro-architected interpenetrating phase composites*.

1.4 Architected composites

The idea of a three-dimensional composite with some degree of architectural design is not by itself new. Woven three-dimensional composites have been studied since the 1990s [33]. A "non-woven" composite architecture was devised by Das and co-workers [34] with the primary benefit of improving the compressive failure response by eliminating fiber kinking due to the wavy nature of woven fibers. However, the fabrication method involves the placement of each individual fiber in a complex three-dimensional arrangement, which makes scaling of the fabrication method difficult, especially if a separation of scales is to be attained. More recent work on interpenetrating phase composites makes use of additive manufacturing, which presents a reproducible, scalable, and freeform fabrication method. Due to the robustness of additive manufacturing, these works cover a wide range of geometries, including beam-based, surface-based, and even aperiodic structures [35, 36, 37, 38, 39]. Together, they demonstrate that architecture may be harnessed to refine, tune, and optimize mechanical performance, achieving outstanding stiffness, strength, and damage resistance.

The main limitations to the existing literature on interpenetrating phase composites are twofold. First, due to the nature of commercially available 3D-printing systems, most architected IPC samples having sub-millimeter scale features are made of polymers. While polymers span a wide range of stiffnesses (Figure 1.1), they are orders of magnitude less stiff compared to carbon, which is the principal structural material used in engineering composite applications, meaning it is difficult to make a direct comparison to existing composite materials in terms of mechanical performance. Moreover, many examples of architected IPCs fail to achieve an adequate separation of scales due to an insufficient number of unit cell tessellations. In particular, when the length scales of architectural features coincide with specimen length scales, the measurement of mechanical performance attributable to material properties is precluded because boundary effects confound the observation of material behavior (e.g., due to the free lateral surfaces or friction from the compression platens).

In this work, we directly address these two shortcomings in order to properly characterize the fabricated micro-architected interpenetrating phase composite *materials*. Specifically, we use fabrication techniques which provide both resolution and scalability to achieve a separation of scales. For example, we achieve the fabrication of samples containing at least $15 \times 15 \times 15$ tessellations of unit cells, far above the convergence value of $5 \times 5 \times 5$ experi-

mentally verified for the geometry under consideration [40].

Moreover, we will first benchmark our composites using a polymer-based system for effective comparison to the current state-of-the-art, then develop a scalable and facile fabrication method for the fabrication of centimeter-scale *carbon-based* composites, enabling a direct comparison of mechanical performance to "traditional" composite materials. Both systems are capable of yielding centimeter-scale specimens with feature sizes on the order of $10-100$ µm, meaning the production of physically meaningful prototyptes is possible. Furthermore, using two material systems enables a thorough investigation of how morphology is tied to mechanical performance in an architected IPC, and how material selection enhances the effect of morphology alone. Altogether, this work aims to develop a fundamental understanding of the mechanical behavior of architected IPCs behave and outline a scalable method for their fabrication, creating the foundation for a new class of strong, resilient, and programmable materials.

1.5 Outline

The remainder of this thesis will detail our findings on the response of three-dimensional micro-architected interpenetrating phase composites in order to understand, predict, and ultimately engineer their behavior, using both computational and experimental methods. In Chapter 2 we discuss the realization of 3D micro-architected IPCs across two material systems, using robust and scalable manufacturing techniques driven by modern additive manufacturing processes. We discuss the characterization of fabricated samples and describe the bulk material properties of the constituent materials used to create the composites. Finally, we briefly discuss the computational techniques used to model and predict the behavior of the fabricated samples.

In Chapter 3 we connect the behavior of two-phase architected composites to the classical construction of bending and stretching in the elastic regime, as first discussed by Gibson and Ashby [13, 41]. We then suggest how the framework of architected composites can challenge the traditional notion of the Maxwell criterion as a necessary condition for a bending-dominated response. We prove that independent of material system, there exists a critical ratio of constituent material properties that can create a stretching-dominated response in a bending-dominated architecture. Using computational and experimental methods, we demonstrate a mechanism for this bending-to-stretching transition and demonstrate its existence in fabricated samples across material systems.

In Chapter 4 we discuss the non-linear response of architected composites, namely the behavior of composites in the regime of finite deformation. We introduce a metric called the *interaction effect* that quantifies the increase in material properties exhibited by the composite over the sum of its constituent parts and we compute the interaction effect for various material systems. Finally, we use X-ray computed tomography (XCT) scans on fabricated samples tested to various strains to understand the progressive nature of failure in the composite Kelvin structure, which leads to the enhancement of mechanical performance quantified by the interaction effect.

In Chapter 5 we extend our knowledge of architected composites to design a unit cell whose behavior in the composite state can be tailored based on a knowledge of geometry and

constituent material properties. As an example of this framework we construct, fabricate, and test a particular minimal pair of architectures whose performance is predictably reversed between the single-material and composite states, and in particular show how a careful geometric design and material selection leads to an enhancement of the interaction effect in a composite.

Finally, in Chapter 6, we provide a summary and outlook on the space of 3D micro-architected interpenetrating phase composites, together with a perspective on promising further research directions.

Chapter 2

Materials and Methods

2.1 Fabrication

In order to study the mechanical behavior of 3D micro-architected IPCs across material systems, we employed two distinct methods to fabricate the architecture phase of the composite: two-photon lithography (TPL) 3D-printing, which created a polymer-based system, and desktop vat photopolymerization (VP) 3D-printing followed by pyrolysis, which yielded a carbon-based system. The Kelvin (regular tetrakaidecahedron) unit cell will be the basis of our investigations. To this end, both fabrication methods produced millimeter-scale or larger architected-material samples consisting of tessellated Kelvin unit cells having sub-millimeter feature sizes; to ensure a separation of scales was achieved, each sample consisted of a minimum of $15 \times 15 \times 15$ tessellations. These single-material structures, which we refer to as the "reinforcing phase", were then infiltrated with a second matrix material to create architected composites.

2.1.1 Materials

For TPL 3D-printing, two-photon photosensitive resin UpPhoto was used as received (UpNano, Vienna, Austria). For VP 3D-printing, poly(ethylene glycol) diacrylate (PEGDA, average molecular weight 700), photoinhibitor Sudan I, and photoinitiator phenylbis(2,4,6-trimethylbenzoyl)phosphine oxide (BAPO) were used as received (Sigma-Aldrich, USA). For infiltration, silicone elastomer Sylgard 184 (PDMS, Dow Corning, USA), urethane resin Smooth-Cast 61D (Smooth-On, USA), and two-part epoxy resin West System 105/206 (West System, USA) were used as received.

2.1.2 Two-photon photopolymerization

Two-photon lithography, also called two-photon polymerization (TPP) or sometimes direct laser writing (DLW), is an additive manufacturing process that uses a pulsed laser to selectively polymerize a liquid-state polymer precursor. It is the highest-resolution 3D-printing process that is commercially available today and is a quickly-growing field of research interest and recently, commercial interest [42, 43].

To create the reinforcing phase for the polymer-based material system, we used the commercially available TPL printer NanoOne (UpNano, Vienna, Austria) to fabricate 20 × 20×20 tessellations of unit cells. The unit cells were designed in a commercial computer-aided design (CAD) software to range from 7% relative density to 22% relative density, although the fabricated specimens were of larger relative density than the nominal values, as a result of the printing process. Each unit cell nominally measured 200 µm in length, so that the nominal specimen size was 4 mm. Structures were printed using a pulsed femtosecond laser operating at 100 mW, scanning at 600 mm s^{-1}. The slicing distance (layer height) was 3.0 µm, and the hatching distance was 2.1 µm. The millimeter-scale specimen was subdivided into 60 µm-tall "blocks" for printing, with a 50% block offset between neighboring blocks. The block offset procedure ensures that the printed structure does not delaminate along stitching lines. Structures were printed onto a cleaned and silanized glass substrate using a 10× objective with the commercially available UpPhoto photopolymer resin. Following the manufacturer's recommendations, printed parts were washed in 2-propanol for a minimum of 30 minutes, followed by drying for a minimum of 24 hours in air. No further post-processing of printed parts was performed.

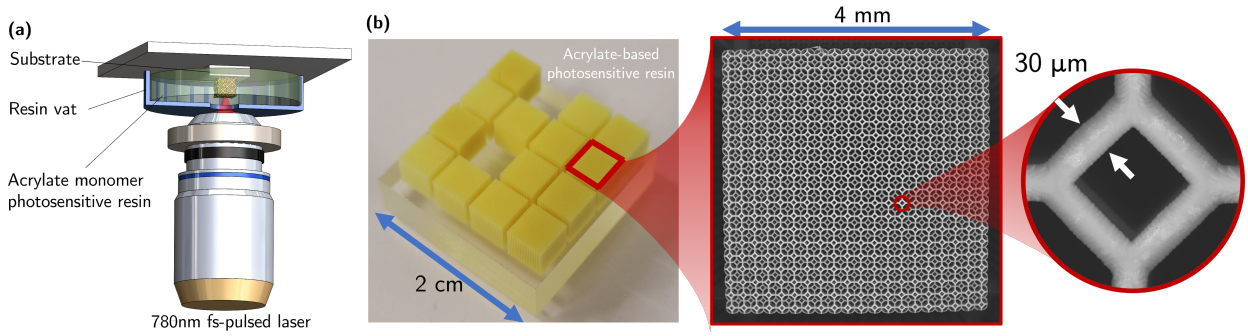

Figure 2.1: Two-photon lithography creates the polymer reinforcing phase. (a) Schematic of the TPL system and (b) photograph of a set of fabricated specimens together with scanning electron microscopy of a fabricated polymer structure, demonstrating a separation of scales.

2.1.3 Vat photopolymerization and pyrolysis

As a second material system, we employed vat photopolymerization using a desktop ultraviolet liquid crystal display (UV LCD) 3D-printer (Phrozen Tech Co., Ltd., Hsinchu City, Taiwan) to create macroscale, polymeric architected structures, which were then pyrolyzed in a vacuum furnace to yield microscale reinforcing phases consisting of carbon.

We designed the carbon specimens, which consisted of 15 × 15 × 15 tessellations of unit cells, at various nominal relative densities ranging from 4% to 12%; however, as a result of fabrication, the realized structures again had relative densities higher than their nominal values, ranging between 8% and 22%. Unlike the TPL structures, which all had the same nominal unit cell size, the carbon reinforcing phase structures were designed to be of the same *mass*, so that the pyrolysis process would be consistent across batches. As a result, the beam thickness and unit cell size (and correspondingly, the specimen size) varied between

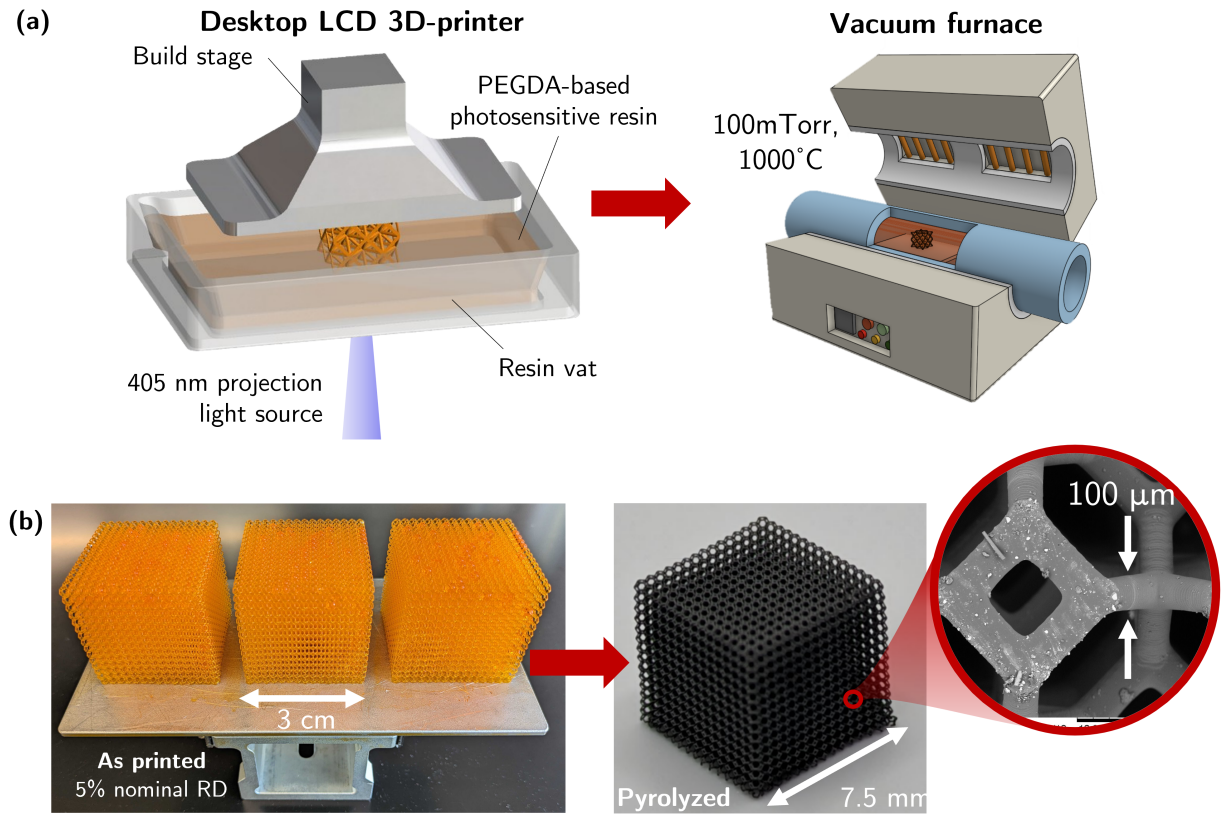

Figure 2.2: Desktop vat photopolymerization followed by pyrolysis creates the carbon reinforcing phase. (a) Schematics of the desktop LCD 3D printer used to fabricate macroscale polymer structures, and the vacuum furnace used for subsequent carbonization. (b) Photographs of a carbon reinforcing phase before and after pyrolysis, with (inset) an SEM micrograph showing detail of the beams, which demonstrates a separation of scales.

specimens. Beam thicknesses ranged between 230 and 310 µm, and unit cell sizes ranged between 1800 and 2850 µm.

The material used to fabricate the polymeric structures for pyrolysis was a custom polyethylene glycol diacrylate (PEGDA)-based photopolymer resin. To create the resin, PEGDA, BAPO, and Sudan I were mixed at a ratio of 100:1:0.1 by mass, followed by ultrasonication for 60 minutes. Upon exposure to light in the UV wavelength range (405 nm), the resin was selectively cured to create centimeter-scale structures. After printing, the PEGDA structures were washed in 2-propanol for a minimum of 12 hours, followed by drying for a minimum of 24 hours in air.

After drying, the PEGDA structures were transferred to a vacuum furnace for pyrolysis. The chamber was evacuated to a pressure no greater than 100 mTorr, and the temperature followed the heating profile in Figure 2.3(b). As a result of the pyrolysis process, the polymer structures experienced an average mass loss of 98% and, on average, linear shrinkage by a factor of 4.5. Consequently, this pyrolysis step resulted in centimeter-scale carbonized specimens having a characteristic beam diameter on the order of 100 μm.

The heating profile in Figure 2.3(b) was chosen after a thermogravimetric analysis (TGA)

on the custom PEGDA-based resin (Figure 2.3(a)) revealed a peak of the mass loss rate within a temperature range of 372°C to 454°C. For this reason, the profile has extended holds at temperatures of 300°C and 400°C with a slow ramp between. After decomposition, pyrolysis takes place up to a maximum temperature of 1000°C. It has been shown [44] that in vacuum, carbon undergoes microstructural changes at temperatures below 900°C, with stabilization above this temperature corresponding with a plateau in the Young's modulus. After a hold at the maximum temperature, the furnace was cooled down to room temperature, at which point the carbonized reinforcing phase structures were removed.

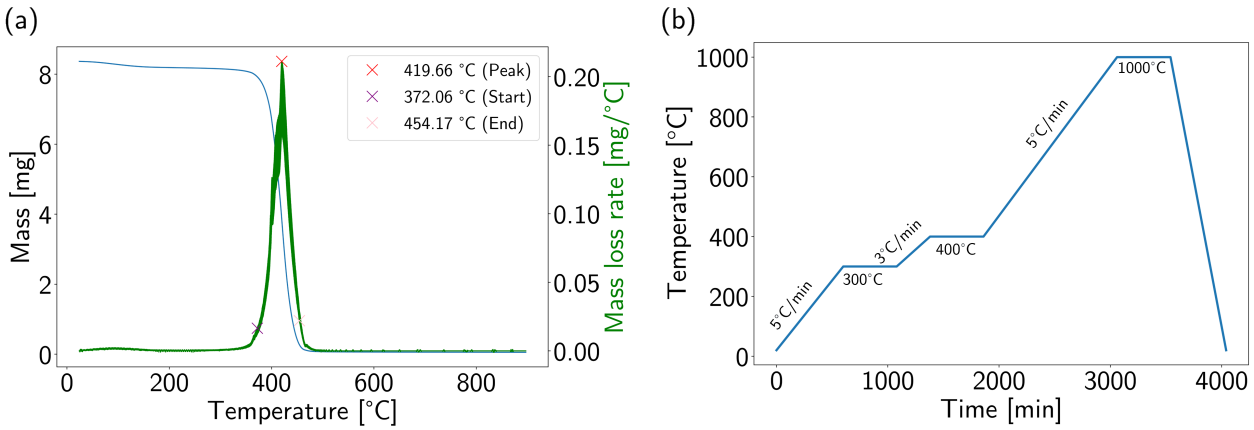

Figure 2.3: (a) TGA curve showing mass loss and mass loss rate for the custom PEGDA resin, and (b) corresponding heating profile used in the vacuum furnace.

2.1.4 Matrix infiltration

Three matrix materials were used: polydimethylsiloxane (PDMS, a silicone elastomer), Smooth-Cast 61D (SC61D, a urethane resin), and an epoxy resin (West System 105/206). Each matrix material consists of a two-part liquid precursor, which undergoes crosslinking and solidification when mixed. Matrix infiltration was accomplished using either vacuum infiltration (for the PDMS and SC61D materials) or centrifuge infiltration (for the epoxy resin, which was too viscous in the liquid state to enable vacuum infiltration). To perform vacuum infiltration, we submerged the printed or carbonized specimens in 10 mL of matrix precursor, followed by evacuation inside a vacuum chamber to a pressure of approximately 5 Torr. Evacuation continued until the pot life of the matrix precursor was nearly reached; then, the sample was extracted from the liquid, the exterior was gently wiped dry to remove excess matrix material, and the sample was then cured according to the manufacturer's instructions. To perform centrifuge infiltration, the matrix material was added to a centrifuge vial containing the printed or carbonized sample. The samples were then centrifuged at 2000 RPM for 5 minutes. The sample was then extracted, gently wiped, and cured. In each case, following complete curing, the infiltration was checked for voids (see section 2.2.2). All composite samples used for mechanical characterization had a volumetric void fraction no greater than 1%.

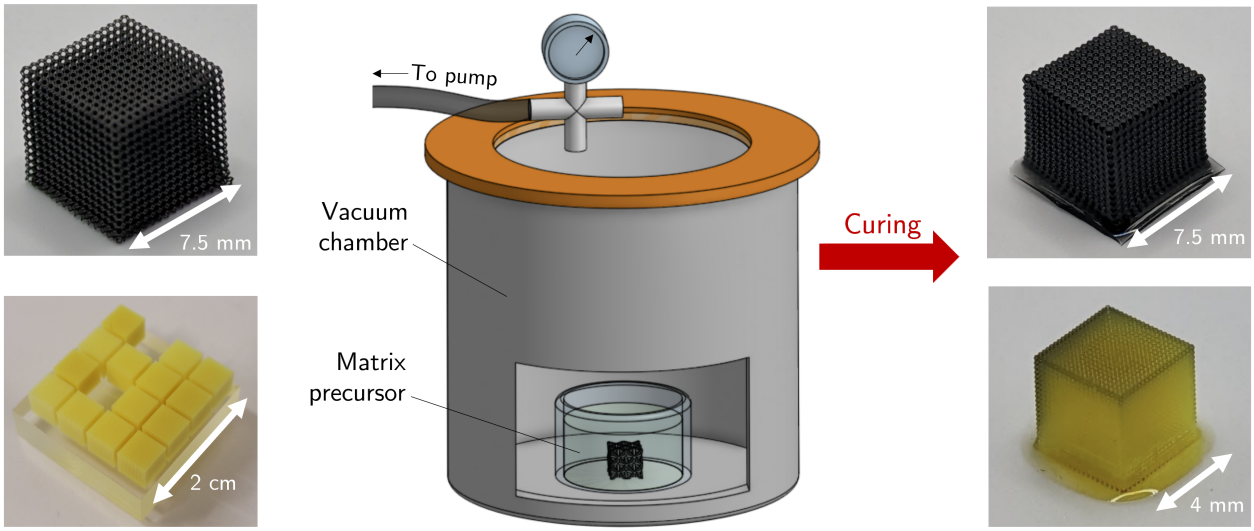

Figure 2.4: Infiltration of the reinforcing phase (e.g., using vacuum treatment) creates architected composites.

2.1.5 Constitutent material properties

We record the constituent material properties of the reinforcing phase for both the polymer system (viz. UpPhoto) and the carbon system (viz. pyrolytic carbon), as well as the matrix materials (PDMS, SC61D, and epoxy resin). To obtain the material properties of UpPhoto and pyrolytic carbon, a commercial nanoindenter (Alemnis Standard Assembly, Switzerland) was used to measure pillars of bulk material.

The indenter was used in uniaxial compression mode to test a pillar of UpPhoto to 50% engineering strain. In the case of the pyrolytic carbon, the indenter was used in nanoindentation mode in conjunction with a Berkovich indentation tip to obtain the reduced stiffness of a pillar, from which the elastic modulus can be obtained [45]. Macroscopically, the pyrolytic carbon was observed to behave in a purely elastic manner, characterized by a catastrophic brittle failure mode. The matrix material properties were obtained using uniaxial compression of cured monolithic cubes with 10 mm side length on an Instron 5900 series testing system.

UpPhoto

Using the particular TPP print parameters established for the present study, polymerized UpPhoto is an elastic-plastic material exhibiting post-yield hardening (Figure 2.5(a)). The elastic modulus was measured to be 2.5 ± 0.2 GPa, and the yield strength was measured to be 92 ± 8 GPa.

Pyrolytic carbon

Using the reduced stiffness method outlined in Ref. [45], the elastic modulus of pyrolytic carbon was measured by Berkovich nanoindentation to be 32 ± 4 GPa (Figure 2.5(b)). This

is in agreement with the range of modulus values for disordered pyrolytic carbon reported in the literature [46]. The load-displacement data from which the elastic modulus was derived is shown in Figure 2.5(b).

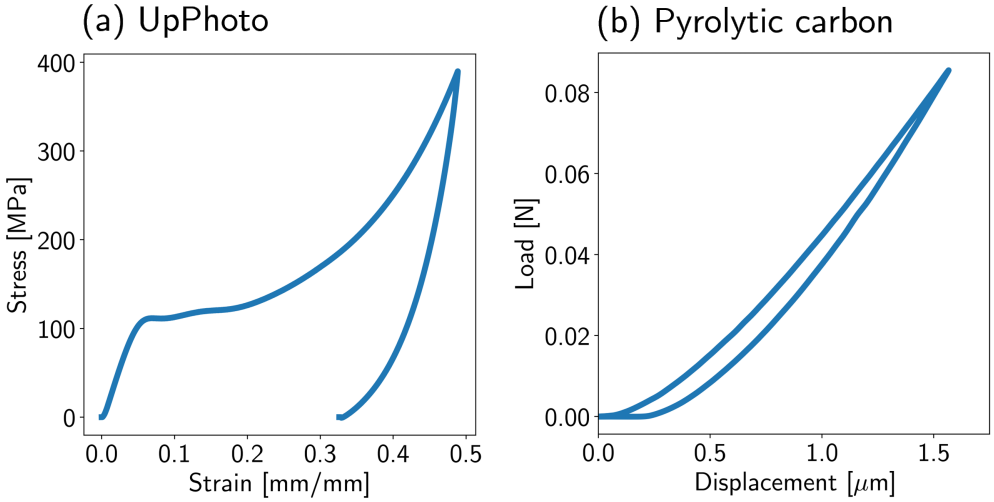

Figure 2.5: Typical compressive mechanical behavior of the constituent materials used for the reinforcing phases. (a) Stress-strain data corresponding to uniaxial compression of a monolithic UpPhoto pillar and (b) load-displacement data corresponding to nanoindentation of a pyrolytic carbon pillar.

PDMS

As prepared in the present study, PDMS exhibited the stress-strain response in Figure 2.6(a) when tested in uniaxial compression. In the limit of small strain, the elastic modulus was 4.1 ± 0.3 MPa. At larger strains, PDMS is commonly modeled as an incompressible, nonlinear hyperelastic material [47]. Our test data fit several incompressible material models well. For example, a fit of the true stress-stretch relationship to the Gent material model reveals best-fit parameters $\mu_0 = 0.982$ MPa and $I_m = 8.804$. A fit to the Arruda-Boyce model (using a five-term approximation to the Langevin function as referenced in the ABAQUS implementation) has best-fit parameters $\mu_0 = 1.337$ MPa and $\lambda_m = 1.488$.

Smooth-Cast 61D

The Smooth-Cast 61D urethane resin exhibited the stress-strain response in Figure 2.6(b), similar to the PDMS response but globally stiffer. The elastic modulus was 80 ± 4 MPa. However, unlike the PDMS this urethane resin cannot be modeled as hyperelastic, exhibiting some permanent deformation when tested to high strains and demonstrating a large amount of hysteresis upon unloading.

Epoxy resin

The epoxy resin, whose response is given in Figure 2.6(c), has an elastic modulus of 845 ± 69 MPa. After the initial linear-elastic regime, the epoxy samples exhibited extremely nonlinear behavior characterized by a drop in load, whereby a network of microcracks were observed in tested samples. Following this load drop, the stress-strain curve suggests slight hardening behavior followed by compaction of the samples in compression. Qualitatively, this behavior is consistent with the compressive behavior of a highly-crosslinked polymer [48].

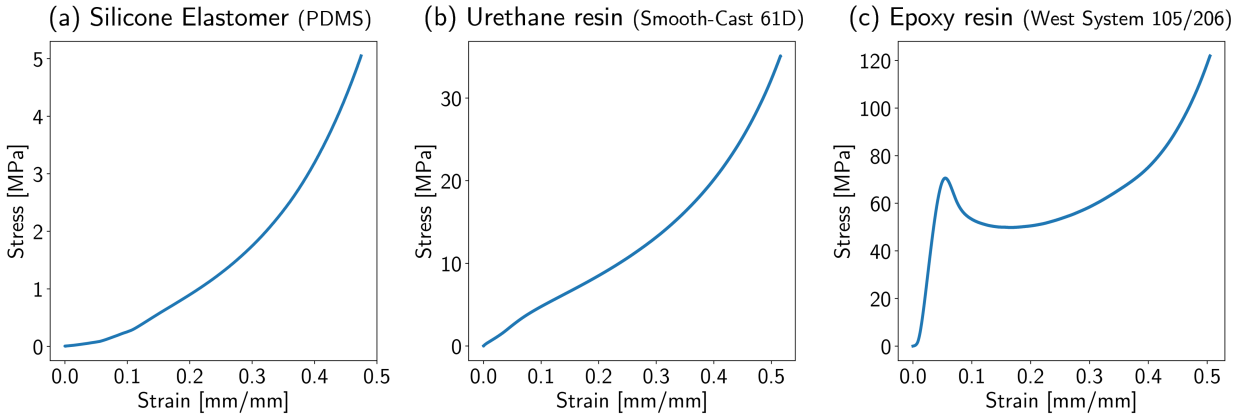

Figure 2.6: Typical compressive mechanical behavior of the constituent materials used for infiltration, all taken from uniaxial compression data of centimeter-scale monolithic specimens: (a) silicone elastomer PDMS, (b) urethane resin Smooth-Cast 61D, and (c) epoxy resin West System 105/206.

2.2 Characterization

2.2.1 Microscopy

Specimens were visually inspected after each fabrication step using optical and scanning electron microscopy. Optical microscopy was used to verify the morphology of features but was not used to make critical measurements. Using a desktop scanning electron microscope (SEM; Hitachi, Tokyo, Japan), micrographs were taken of each specimen at a minimum of three distinct locations across its exterior faces. A commercial image analysis software (ImageJ, National Institutes of Health/LOCI, University of Washington) was used to measure beam thicknesses and unit cell sizes. An average of at least three measurements was used to compute the as-fabricated beam thickness and the unit cell size for each sample, in order to obtain a measurement of the true relative density. To prevent the build-up of charge on non-conductive samples, the polymer lattices were coated in a thin layer ($\approx$ 10 nm) of gold using a sputter coater (Oerlikon Balzers, Liechtenstein).

2.2.2 X-ray computed tomography

X-ray computed tomography (XCT) of samples before and after mechanical testing was performed using a Versa 620 X-ray microscope (Zeiss, Germany). Samples were mounted on a graphite sample holder. X-rays were generated at 60 kV with a total power of 6.50 W and 4-second exposure scans were taken using the 0.4× objective with a voxel size of 7.65 µm. Post-processing and three-dimensional reconstruction was performed with a commercially available software suite from the manufacturer. Each reconstruction was computed using 1601 scans.

2.2.3 Uniaxial compression testing

Mechanical testing in uniaxial compression was undertaken on an Instron 5900 series universal testing system (Instron, USA). The polymer-based system was tested using a 1 kN load cell in order to maximize sensitivity; the carbon-based system reached higher ultimate loads under uniaxial compression and required a 50 kN load cell. All samples were tested under displacement control at a strain rate not exceeding 10^{-3} s^{-1}. Load and displacement data were recorded and exported and converted to engineering stress and engineering strain data, respectively, using measured specimen dimensions.

Following the ASTM standard protocol for uniaxial compression [49], the elastic (Young's) modulus of each sample was extracted using a least-squares regression linear fit on the initial portion of the stress-strain curve, excluding any initial "toe" region corresponding with machine and sample compliance. The yield strength of each sample was extracted using the 0.2%-offset method. The toughness of each sample was extracted by numerical integration of the stress-strain data.

2.3 Simulation

Finite-element analysis of architected composite unit cells was carried out using the commercial software ABAQUS. Geometries were exported from CAD software as solid body (.STEP) files (Figure 2.7(a)), and imported into ABAQUS as such, ensuring that meshing could be done from scratch in ABAQUS. The two phases of the composite were imported as separate solid body files called the "positive" phase and "negative" phase. After the import process, material properties (e.g., as extracted from uniaxial compression tests, section 2.1.5 above) were applied to each phase separately. Then, the positive and negative geometries were joined using a Boolean operation which preserved the geometrical boundaries and material assignments between the phases. The combined body was meshed using second-order (ten-node) tetrahedral elements (C3D10). In the case of an incompressible matrix material (e.g., PDMS), second-order tetrahedral elements with a hybrid formulation (C3D10H) were used instead. These C3D10H elements contain an additional internal variable associated with the arbitrary hydrostatic pressure admitted by an incompressible material. The ideal mesh seed size was found as a result of a mesh convergence study. The mesh seed size was a function of the beam thickness t; the convergent seed size was found to be $t \times (0.3/1.1)$. This seed size resulted in four mesh elements being created across the diameter of each beam, regardless

of the absolute beam size (Figure 2.7(b)). The number of elements used thus varied across geometries, but was typically on the order of 10^6 for a composite Kelvin cell (Figure 2.7(c)).

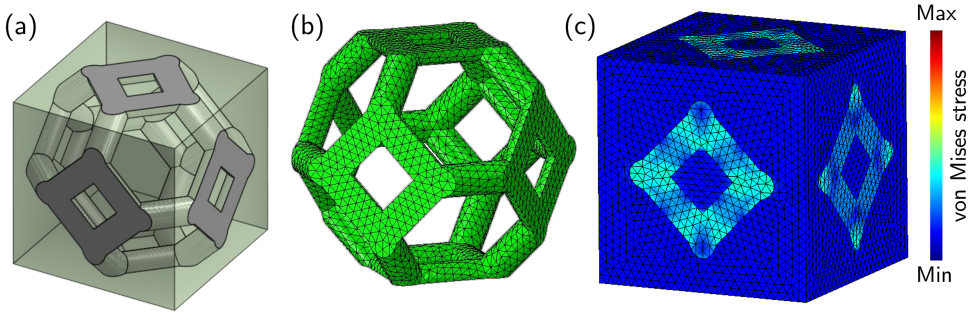

Figure 2.7: Finite element simulation of the architected composites. (a) Solid body models of the positive (gray) and negative (green) phases were created separately in a CAD software package. (b) Example mesh of the positive phase, with seed size determined by a mesh convergence study. (c) Example finite element simulation result showing the distribution of von Mises stress due to a linear perturbation to 1% compressive strain.

To simulate a quasi-infinite tessellation of each unit cell under consideration, we applied a periodic mesh and enforced periodic boundary conditions (PBCs) to the unit cell [50]. The periodic mesh ensures that for all nodes on the unit cell boundary $\delta\Omega$, a given node m on any face of the unit cell matches up with exactly one node n on the opposite face of the same unit cell, and the PBC is the additional constraint that the *relative* displacement between the nodes is a *constant*. This constant is specified by the (macroscopic) displacement gradient $\mathbf{H}$, which is related to the macroscopic deformation gradient $\mathbf{F}$ by the relationship $\mathbf{H} = \mathbf{F} - \mathbf{I}$. Specifically, the extra constraint equations for a node-pair read

$$\mathbf{u}(m) - \mathbf{u}(n) = \mathbf{H}\left\{\mathbf{X}(m) - \mathbf{X}(n)\right\}, \tag{2.1}$$

where $\mathbf{X}(i)$ denotes the position of node i in the reference configuration. In order to replicate the displacement-controlled experiments, we implemented the constrain equations using "dummy nodes", which are virtual nodes that are not themselves part of the continuum but are still considered by ABAQUS to solve the system. We defined the dummy nodes at an arbitrary spatial location and enforced the local displacement of these nodes exactly according to the desired macroscale deformation. An additional fixed dummy node was included with the effect of preventing rigid-body motion of the continuum.

To find the resultant stress on the body, the principle of virtual work is used to relate the external virtual work of the dummy nodes (in enforcing the prescribed displacement) and the internal virtual work of the continuum (in responding to the prescribed displacement) [50, 51]. This relation, together with contours of stress and displacement components throughout the body, provides insight into the mechanical behavior of the unit cell, for example highlighting stress transfer pathways within the matrix.

Chapter 3

Elastic behavior

In the elastic regime, the classic scaling-law argument (1.4) suggests that stiffness and density are related linearly in the case of a stretching-dominated architecture and quadratically in the case of a bending-dominated architecture. As discussed in Chapter 1, one fundamental assumption used in deriving these results is that the architecture is constructed from slender beams. However, implicit in the discussion of this beam-based architectural behavior is the additional assumption that the unit cell is filled with air, and that any deformation of beams is constrained only by kinematics and the elastic properties of the architecture's constituent material.

We now pose the question: how does the addition of a *load-bearing matrix phase*, as in an IPC, affect the stiffness-density relationship in an architected composite — in particular, for a bending-dominated structure like the Kelvin cell? Specifically, how might the relative stiffnesses of the two material phases change the response of the composite?

3.1 Effect of the stiffness fraction E_m/E_f

In accord with existing literature on composite materials, we denote the Young's modulus of the architecture phase as E_f, and the Young's modulus of the matrix (reinforcement) phase as E_m. We will assume that $E_m \leq E_f$, as is typical for two-phase composites. Let the effective stiffness of the *composite* be E_c. Our goal is to see how E_c changes with the stiffness fraction E_f/E_m when the entire unit cell is within the elastic regime. To this end, we simulated the response of a Kelvin cell to a linear perturbation (at 1% strain).

Figure 3.1(a) shows the composite stiffness E_c normalized by E_f, as a function of the relative density of the architecture, for the two extreme cases of $E_m/E_f = 0$ (achieved, for example, when there is no matrix) and $E_m/E_f = 1$ (achieved, for example, when the matrix and architecture consist of the same material). When $E_m/E_f = 0$, we obtain an exponent of $m = 2.182$ (which appears as the slope on this log-log plot), close to the value of 2 predicted by the "classical" bending-dominated, single-material scaling law; when $E_m/E_f = 1$, the relative density is irrelevant and the composite stiffness is exactly E_f, and hence the scaling exponent is zero. Given that $0 < E_m/E_f < 1$ for any composite, we must have $0 < m < 2.182$; this "achievable design space" is indicated by the shaded region in figure 3.1(a).

Next, the stiffness fraction E_m/E_f was varied among six distinct values between 0 and

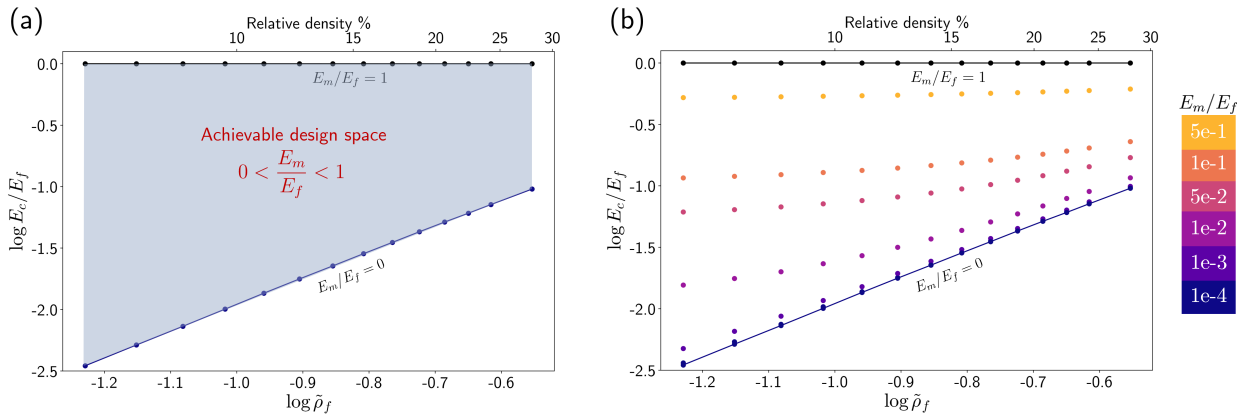

Figure 3.1: Simulation of a composite Kelvin cell to a 1% compressive strain linear perturbation reveals (a) a design space whereby the normalized composite stiffness E_c/E_f depends on the relative density and on the stiffness fraction E_m/E_f but always lies between the unfilled case and the stiffness-matched case. (b) In particular, for various values of E_m/E_f, the log-log plot of composite stiffness versus relative density reveals a change in scaling behavior.

1 (Figure 3.1(b)). As expected, the normalized composite stiffnesses lie within the bounded region, increase with increasing stiffness ratio, and increase with relative density. It can also be seen from Figure 3.1(b) that for a given relative density, as the stiffness fraction increases, the corresponding slope on the log-log plot decreases (Table 3.1). In particular, in the slender-beam limit, the slope — which corresponds to the exponent in the scaling law, (1.4) — decreases from 2.182, for $E_m/E_f = 0$, to zero, for $E_m/E_f = 1$. Also evident in the plot is the regime where nodal effects and non-slender behavior in the architecture dominate, characterized by a change in the apparent slope in the stiffness-density trends. In this regime ($\tilde{\rho} \gtrapprox 12\%$), it remains difficult to ascribe material behavior to a purely bending-dominated or a purely stretching-dominated mode. In Table 3.1, we denote the exponents in this regime by $\hat{m}$.

Stiffness fraction E_m/E_f	Scaling exponent m ($\tilde{\rho} \leq 12\%$)	Exponent $\hat{m}$ ($\tilde{\rho} > 12\%$)
0	2.182	2.084
1×10^{-4}	2.140	2.083
1×10^{-3}	1.885	2.020
1×10^{-2}	0.948	1.615
5×10^{-2}	0.377	0.907
1×10^{-1}	0.248	0.606
5×10^{-1}	0.063	0.140

Table 3.1: Computed scaling-law exponents m for the composite Kelvin cell as a function of stiffness fraction E_m/E_f. In each case, the exponent changes above a critical relative density of 12%, where the slender-beam assumption fails to be satisfied; this secondary exponent is denoted $\hat{m}$.

Importantly, as a consequence of intermediate value theorem, and as revealed by the plot in Figure 3.1(b), or there exists a *critical* stiffness fraction $(E_m/E_f)^*$ for which (in the slender-beam limit) $m = 1$. In particular, Table 3.1 shows that this critical stiffness fraction is close to but slightly less than 10^{-2}.

The classical theory of architected materials says that (1.2) implies (1.4); that is, *if* a slender beam is in a stretching mode, *then* there is a linear scaling between relative density and effective stiffness. Here, we see that for the composite Kelvin cell with $E_m/E_f = 10^{-2}$, a linear scaling appears to exist. Does this imply this critical stiffness fraction is enough to induce stretching?

3.2 A look inside

To answer this question, we consider an even simpler architecture, Figure 3.2. This architecture is inspired by the two-dimensional "minimal example" of Deshpande, Ashby, and Fleck [10], expanded to a three-dimensional unit cell. This unit cell fails to satisfy the Maxwell criterion and is thus bending-dominated. Moreover, if the nodes were pinned, a zero-stress mechanism would exist whereby the lateral nodes would tend to displace outward. Observe that this mechanism, and thus the bending-dominated behavior, would be removed by the presence of lateral beams connecting opposite pairs of nodes, orthogonal to the direction of applied displacement as shown. These "missing" lateral beams would then carry stress when the displacement is imposed.

We perform the same linear perturbation simulations as before, with the same geometrical assumptions. Moreover, we choose a low relative density (4%), well within the slender-beam limit for this particular architecture. To investigate the behavior of the beams, we make a cut along the section plane indicated in the figure and define a local coordinate system whereby the $\mathbf{e}_1^*$-direction is oriented along the beam. With respect to this system, we then resolve the state of stress in the beam and look at the σ_{11}^* component, i.e., the component of normal stress in the direction of the beam.

If the beam is in a state of bending, we would expect the presence of a neutral axis within the beam cross-section, with part of the beam experiencing a tensile σ_{11}^* while the other part of the beam experiencing a compressive σ_{11}^*. Conversely, if the beam is in a state of stretching, we would expect the entire cross-section of the beam to have the same sign of σ_{11}^*.

As shown in Figure 3.2(b), when the stiffness fraction is subcritical (i.e., below 10^{-2}; here, the case of $E_m/E_f = 10^{-5}$ is illustrated), the neutral axis is present, indicating that the beam is in a state of bending. The neutral axis in the case $E_m/E_f = 10^{-5}$ coincides with the geometric centroidal axis of the beam, in accord with the expected behavior of the beam if there were no matrix material, i.e., in the limit $E_m/E_f \to 0$. On the other hand, at the critical stiffness fraction $E_m/E_f = 10^{-2}$, the neutral axis disappears entirely, and the entire cross-section experiences compression. This demonstrates that the critical stiffness fraction does indeed create a state of stretching within the beam even in a geometry that is kinematically non-rigid. An intermediate value of the stiffness fraction (e.g., $E_m/E_f = 10^{-3}$) reveals a *shifted* neutral axis, suggesting a superposed state with characteristics of both bending and stretching. Indeed, it is not until the critical stiffness fraction is reached that

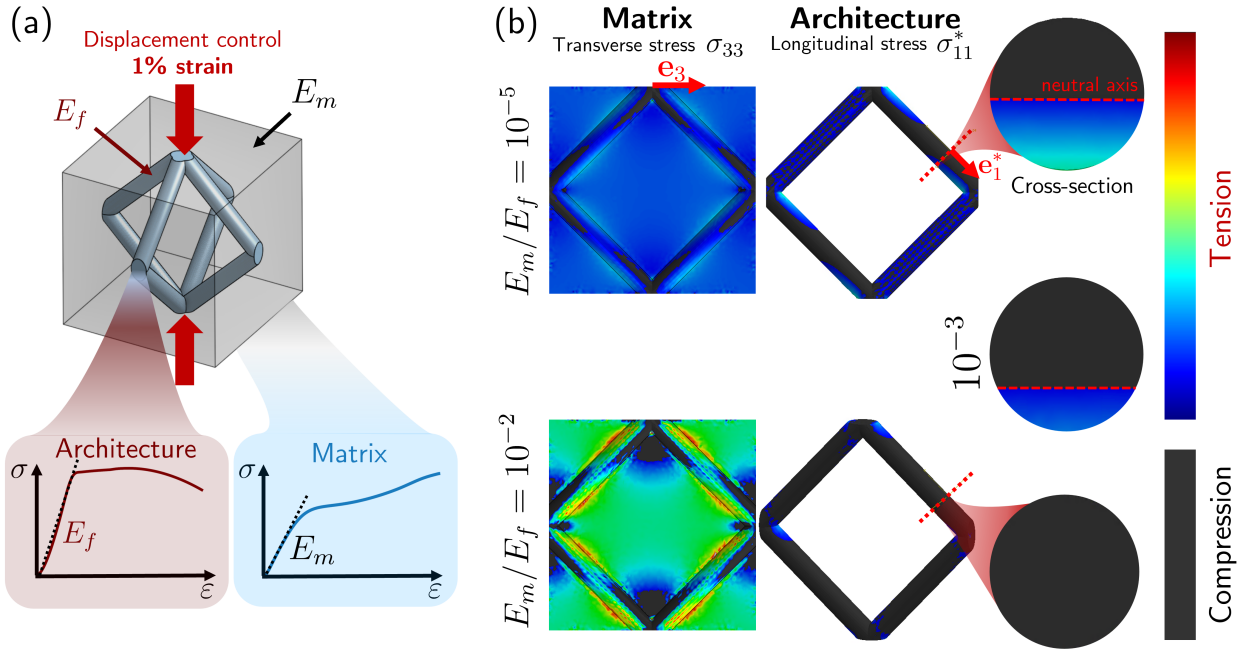

Figure 3.2: Linear perturbation simulations for the three-dimensional minimal example geometry (a), seeded with moduli E_f and E_m (only the elastic properties are considered here). (b) Results demonstrate that for this slender beam structure, the critical stiffness fraction of $E_f/E_m = 10^{-2}$ creates a state of pure stretching in the beams, accompanied by an increase in transverse load carried by the matrix.

the entire beam experiences pure stretching.

To understand why, it is instructive to view the stress distribution in the *matrix*. Specifically, shown in Figure 3.2 is the transverse component of normal stress within the matrix, denoted σ_{33}. At the subcritical stiffness fraction $E_m/E_f = 10^{-5}$, the matrix is subject to a low, roughly homogeneous state of stress. However, when the stiffness fraction is increased to the critical $E_m/E_f = 10^{-2}$, the matrix is able to carry more transverse load. In particular, a load transfer pathway across the middle of the unit cell is established. We hypothesize that the establishment of this load transfer pathway acts like the "missing" beam in the kinematically rigid architecture, and explains the transition from bending to stretching.

3.3 Experimental validation

In order to validate the proposed stiffness fraction-dependent behavior, we performed uniaxial compression tests on the fabricated samples, both unfilled and infiltrated. The unfilled samples represented the case where $E_m/E_f = 0$, whereas the three types of composite specimens had stiffness fractions between 1×10^{-3} and 5×10^{-2}, representing values below and above the proposed critical value. Moreover, the presence of two material systems (viz. polymer-based and carbon-based) allows us to verify whether the critical stiffness fraction condition, which requires only that a nondimensional ratio of moduli attains a particular value, is independent of material system and therefore a property of all architected IPCs.

By performing a best-fit regression to the initial, linear regime of the experimentally determined stress-strain curves, it is possible to plot E_c/E_f as a function of relative density for all experimental samples, Figure 3.3.

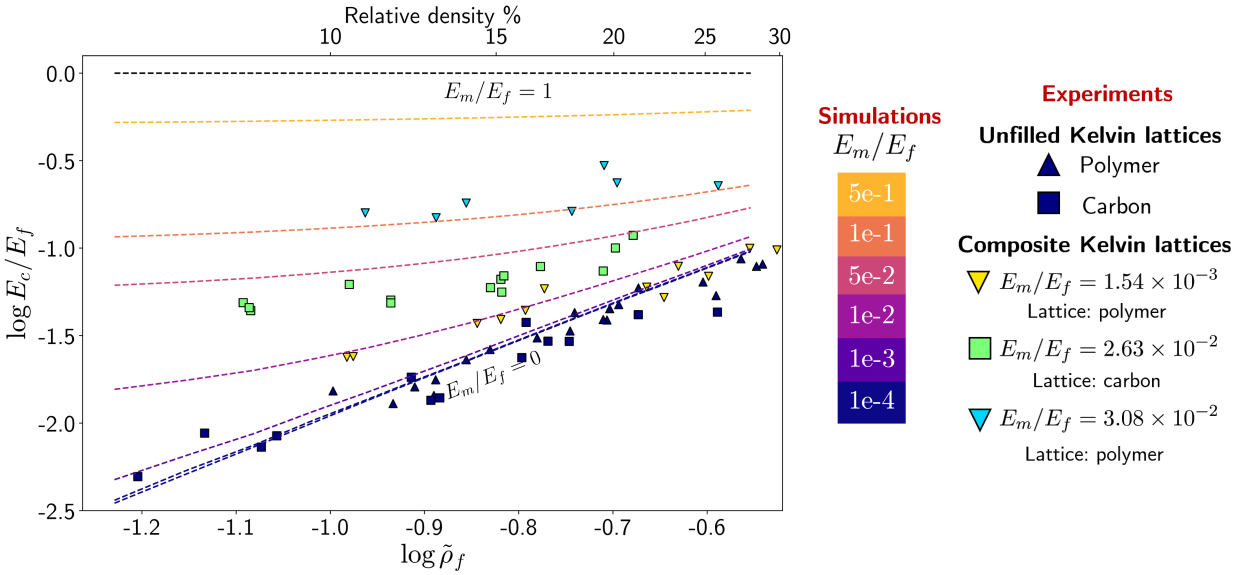

Figure 3.3: Experimentally obtained values of the normalized composite stiffness E_c/E_f against relative density for the two architected precursors (i.e., unfilled lattices) and three architected composites of various stiffness fractions, overlaid atop reference data from simulations (dashed curves).

In the case of unfilled lattices (i.e., architected precursors tested alone), both the polymer and the carbon systems demonstrated good agreement with the corresponding single-material result from simulation (dark-blue triangles and dark-blue squares, respectively). The experimental response of the composite lattices demonstrates stratification based on stiffness fraction, as expected. The polymer-PDMS system (yellow inverted triangles) had a sub-critical stiffness fraction of 1.54×10^{-3}, and the resulting datapoints lie only slightly above the single-material data, in good agreement with the simulation prediction for a stiffness fraction of 1×10^{-3}. The best-fit scaling exponent in this case was 1.307, suggesting that fully stretching-dominated behavior was not achieved.

For the carbon-epoxy system (green squares; $E_m/E_f = 2.63 \times 10^{-2}$) and the polymer-SC61D system (blue inverted triangles; $E_m/E_f = 3.08 \times 10^{-2}$), the critical stiffness fraction was achieved. Correspondingly, the resulting experimental datapoints lie above the $m = 1$ line; best-fit exponents were 0.672 and 0.602, respectively, confirming stretching-dominated behavior. Importantly, however, most fabricated specimens had relative densities outside the slender-beam regime, so the scaling exponents here do not directly imply a state of pure bending or pure stretching. Rather, the observed trends from experiment support the overarching conclusion that a higher stiffness fraction introduces an alternative stress pathway in the matrix which *tends to*, but in the case of a non-slender beam cannot *fully*, change the stress state in the architecture.

Altogether, experimental results corroborate the trends established in the simulation re-

sults, proving the existence of a critical stiffness fraction $(E_m/E_f)^* = 10^{-2}$ whereby independent of material system, a "bending-to-stretching" transition is achieved. Namely, this critical stiffness fraction represents a threshold material property past which stretching-dominated behavior is exhibited in slender composite structures that fail to satisfy the Maxwell criterion in the absence of a matrix material.

Chapter 4

Non-linear behavior

We now turn to study the behavior of the fabricated architected composites past the elastic regime, in order to further understand how load is transferred and damage is propagated throughout the material as strain is increased. To contextualize the performance of our architected composites for both the polymer and carbon material systems, we begin in each case by studying the mechanical behavior of the unfilled architectures.

4.1 Polymer system

As discussed in section 2.1.5, the polymer-system architecture material UpPhoto is an elastic-plastic material when tested monolithically. We created two polymer-based composites: one infilled using the silicone elastomer PDMS, and the other infilled using a urethane resin Smooth-Cast 61D.

4.1.1 Single-material mechanical behavior

Figure 4.1 shows typical stress-strain responses of the UpPhoto Kelvin cell for three relative density regimes we identified as a result of testing. Qualitatively, we found that the behavior of the single-material polymeric Kelvin cell under uniaxial compression is characterized by two principal effects: the presence of horizontally-oriented compaction bands (also called compression bands), and the development of diagonally-oriented shear bands (Figure 4.2). If the compaction band effect dominated, the specimen acted like an open cell foam and exhibited a long plateau period before ultimate densification at a critical strain. Conversely, if shear-banding-dominated, catastrophic failure by fracture occurred once a critical stress was reached. In this way, compression banding results in *strain-limiting* failure, whereas shear banding results in *stress-limiting* failure. The relative dominance of these two effects was found to be dependent on the relative density of the specimen.

The low relative density regime ($\tilde{\rho} \lessapprox 12\%$, Figure 4.2(a)), which is compaction-dominated, is characterized by a long plateau regime at low stress, followed by densification at high strains. These samples developed compaction bands oriented horizontally across the specimen, orthogonal to the direction of compression. The resulting compaction behavior was layer-wise (Figure 4.2(b)), and the order of compacted layers was not deterministic; rather,

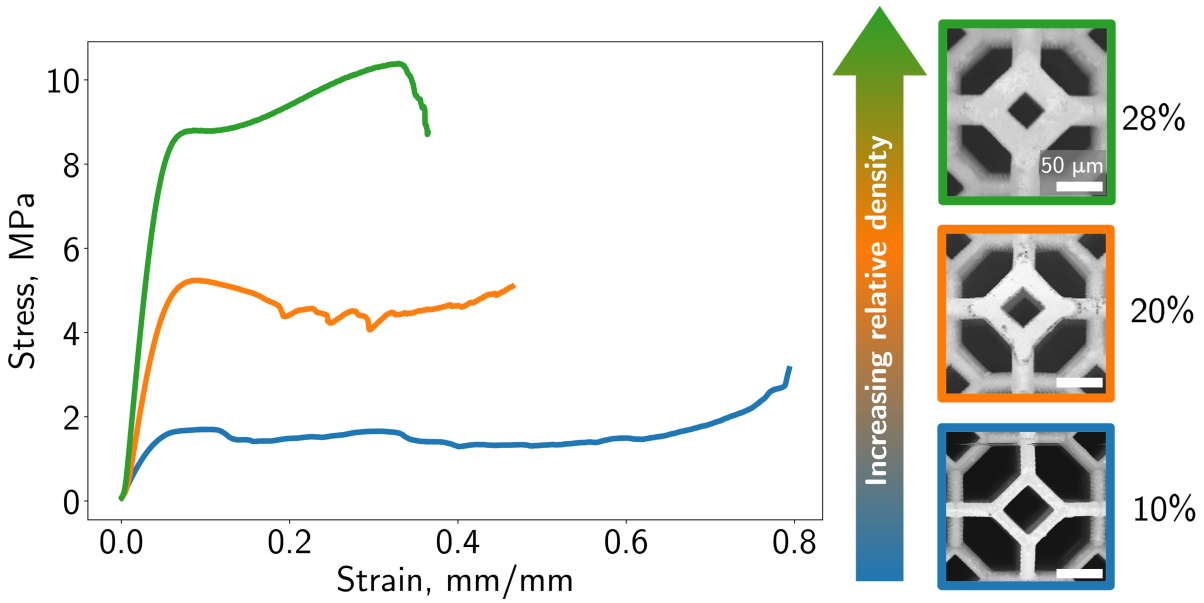

Figure 4.1: Uniaxial compressive behavior of the UpPhoto reinforcing phase at different relative densities. The low relative density regime is characterized by foam-like plateau-densification behavior, whereas a catastrophic fracture event characterizes the behavior at higher relative densities. Intermediate relative densities exhibited an extended plateau regime followed by fracture.

compaction bands likely nucleated from randomly distributed defects in the lattice. This is also evident from the presence of small-amplitude undulations in the stress-strain data, indicating the presence of local crushing instabilities. A small degree of shear banding was evident, characterized by the development of long-range cracks along planes oriented at 45° to the compression direction (Figure 4.2(c)). This shear banding effect, however, was secondary to the compaction behavior.

At higher relative densities ($\tilde{\rho} \gtrapprox 22\%$, Figure 4.2(d)), the stress-strain behavior is characterized by a high sustained stress post-yield, followed by catastrophic loss of load capacity associated with the development of macroscopic cracks along shear bands (Figure 4.2(e)-(f)), leading to a global fracture mode. We hypothesize that these shear bands nucleated from the top and bottom of the specimens, as a result of the triaxial state of stress there originating from compression platen friction. The shear band is only a few unit cells wide, and unit cells located a distance away from the shear band do not experience local deformation, in contrast to the compaction-dominated low-relative-density sample.

Intermediate relative density samples ($12\% \lessapprox \tilde{\rho} \lessapprox 22\%$) exhibited stress-strain behavior with a sustained plateau load, past the typical failure strain of the high relative density samples, but physical behavior indicative of shear-band-dominated deformation corresponding to ultimate failure by fracture, not densification. In this way, the intermediate relative density regime can be considered a transition regime between the compaction-dominated lower relative density regime and the shear-dominated higher relative density regime. Figure 4.3 shows a typical specimen in this intermediate relative density regime that was taken to a strain just before ultimate failure. The development of a shear band is clearly demonstrated

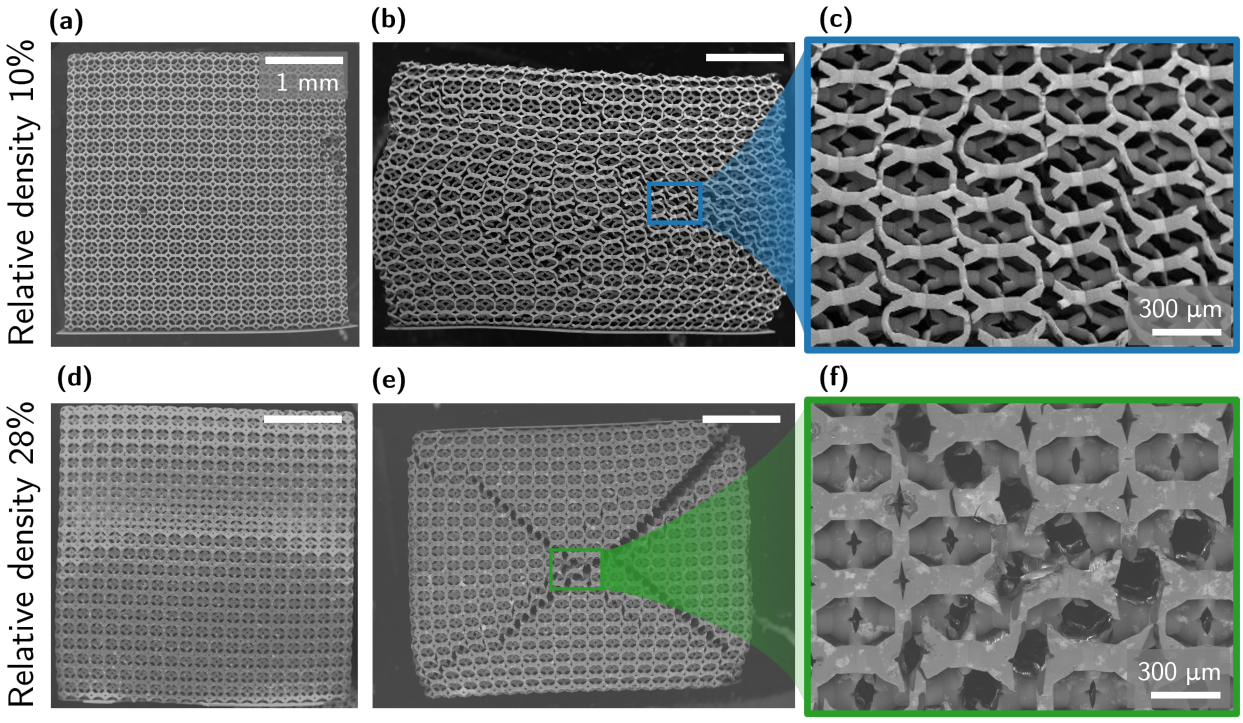

Figure 4.2: Scanning electron micrographs of typical low- and high-relative density UpPhoto reinforcing phases demonstrating both compaction banding and shear banding effects. At low relative densities (a), compaction dominates (b), although shear banding is visible in the ultimate fracture pattern (c). At high relative densities (d), shear banding dominates (e-f), with compaction a secondary effect. Scale bars in (b), (d), and (e) measure 1 mm.

prior to the nucleation of a through-sample crack. The shear bands in these samples were more localized than the shear bands found at higher relative densities (cf. Figure 4.2(e)). Within each unit cell inside of the shear band, cracks nucleated at the corners of beams at the edge of the unit cell (Figure 4.3(c)), where the sharp corner acted as a stress concentration. This type of crack development is consistent with observations on the Kelvin cell as previously described in the literature [52, 39].

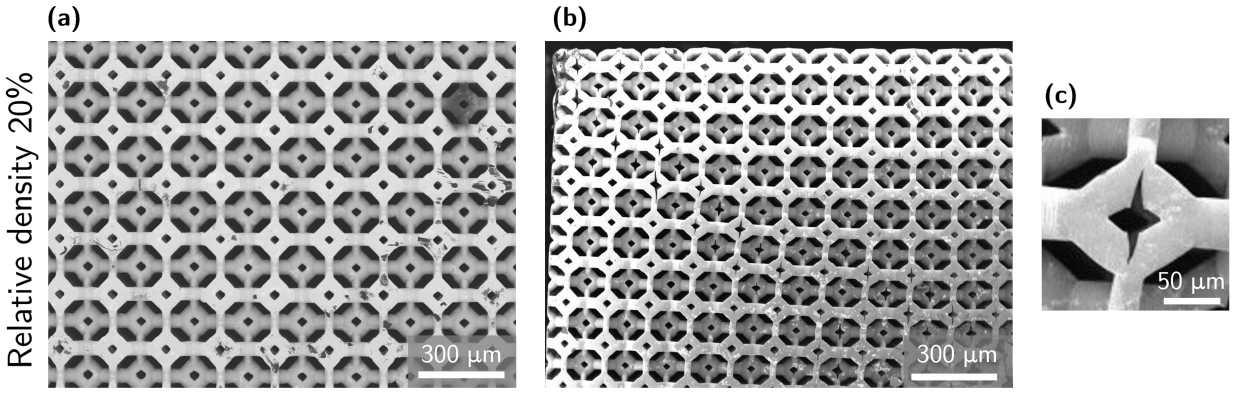

Figure 4.3: At an intermediate relative density (a), scanning electron micrographs of a typical UpPhoto reinforcing phase sample reveal a localized type of failure with cracks progressing along a shear band. This sample was taken to a strain before ultimate failure in order to visualize the growth of cracks within the shear band region.

4.1.2 Composite mechanical behavior

In the case of the polymer-PDMS composite system, two distinct regimes exist, and the intermediate (transition) regime is not present. Figure 4.4 shows two representative stress-strain curves, one from each regime. Clearly, the lower relative density ($\tilde{\rho} \lessapprox 18\%$) specimens are dominated by a densification-compaction behavior in the architecture, which remains stable to high strains, whereas at higher relative densities fracture still controls the ultimate strain.

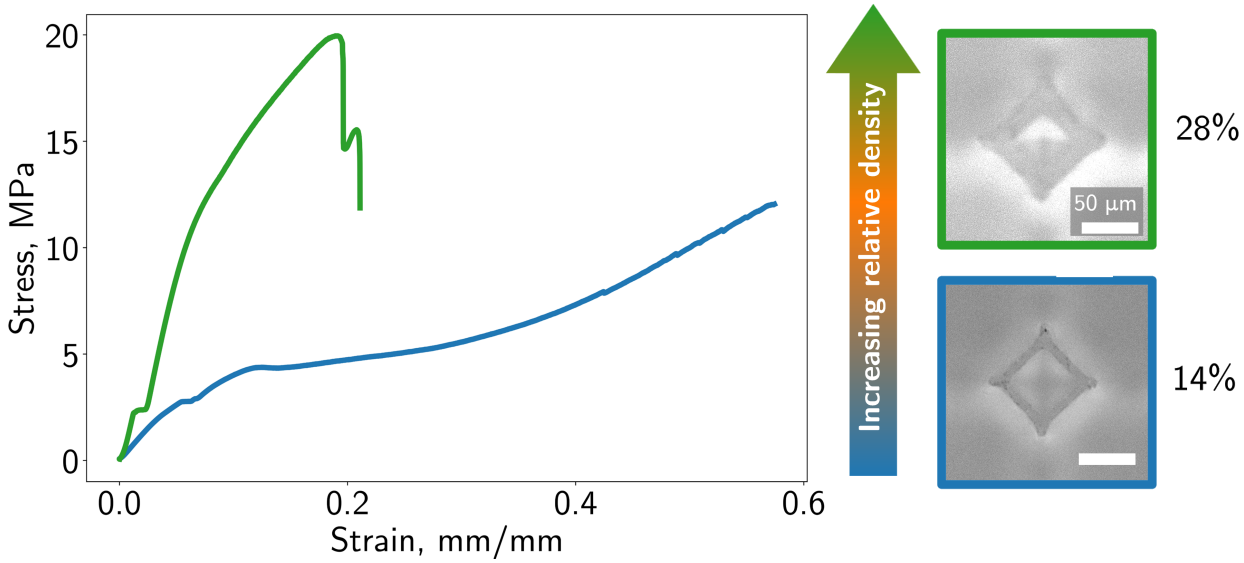

Figure 4.4: Uniaxial compressive behavior of the UpPhoto-PDMS architected composite system reveals two regimes of mechanical behavior separated by relative densities. At lower relative densities, compaction dominates, whereas at higher relative densities, sudden fracture occurs.

In the lower relative density regime, in contrast to the single-material case, the stress-strain curve appears to be monotonically nondecreasing, suggesting that the deformation in the composite leads to a stable load-transfer mechanism. That is, although damage is accruing in the architecture as deformation proceeds in the composite, local load-carrying capacity is never lost due to effective load transfer by the matrix.

In particular, the composite stress-strain curve has a marked slope change near 10% strain, indicating that some type of specimen-scale damage is occurring. This agrees with the observation seen in the single-material case, where the reinforcing phase alone reaches its plateau stress (cf. Figure 4.1). In the case of the composite, however, although critical damage has accumulated in the architecture at this point, the presence of the matrix phase suppresses the foam-like compaction mechanism, marked by a plateau stress, that would otherwise occur. Instead, we see a "stable compaction" accompanied by an increase in load capacity.

The post-mortem SEM micrograph (Figure 4.5) further reveals how the nature of the deformation leads to high composite toughness. In the sample, fracture occurs across a wide band, in contrast to the localized shear or compaction bands seen in the single-material case. Fracture occurs at the 45° planes indicative of shear-band type failure, but also near-vertically across the middle of the specimen, so the shear-band failure pattern does not exist alone in the composite. Moreover, examining the fracture pattern across the composite suggests that the creation of cracks involves a large amount of matrix tearing, a process which requires a large amount of energy. Each individual crack path is tortuous, and this process allows multiple cracks to form and develop before they join near the center of the specimen. This contributes to the high strain and thus high energy needed to cause ultimate failure in the composite.

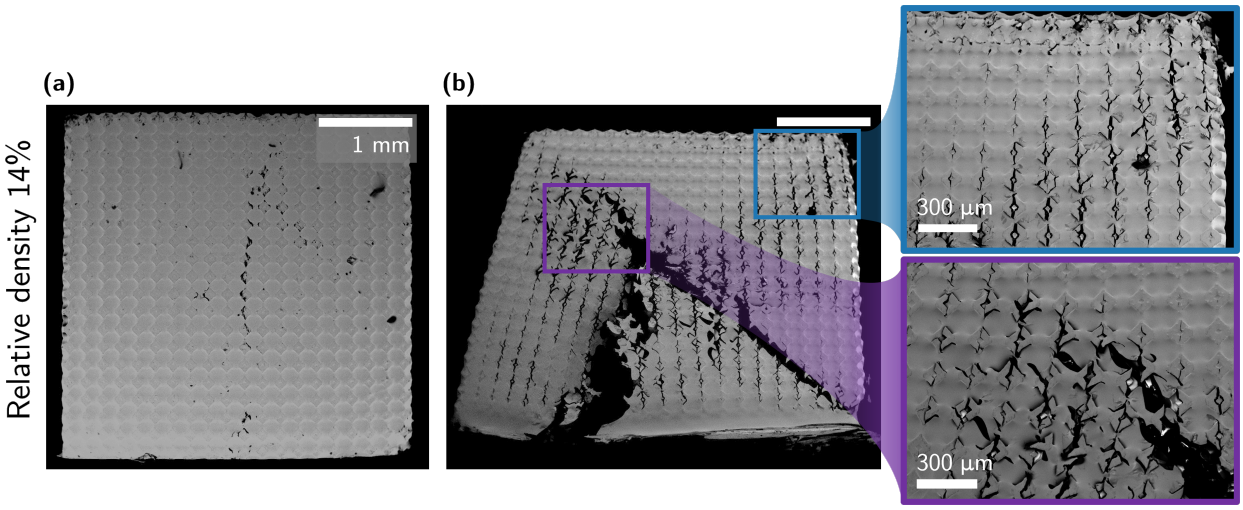

Figure 4.5: Scanning electron micrographs of a low relative density UpPhoto-PDMS composite before and after compression to approximately 60% strain. The scale bar in (b) measures 1 mm. The compaction effect is suppressed by the presence of the matrix phase, and the subsequent development of a tortuous specimen-scale crack involves matrix tearing, leading to high energy dissipation.

In contrast, at higher relative densities, the fracture of the architecture phase continues to dominate. Because the beams in these samples are much thicker, a higher stress—and therefore a higher strain—is required to cause fracture. Additionally, the composite can reduce the effects of internal defects due to the load-transfer capability of the matrix, further increasing the critical strain to failure. The failure pattern in the composite is similar to that of the high relative density single-material case (Figure 4.6, cf. Figure 4.2(e)). However, the fracture mode in the composite case here requires the tearing of the matrix in addition to the fracture of the beams in the architecture. Therefore, in the composite case, the ultimate strength is nearly double that of the single-material specimen. Another consequence of the requirement for fracture across both phases, a direct result of load transfer, is the catastrophic nature of failure, indicated by the sudden drop in load experienced by the composite once the onset of failure happens. Whereas the single-material polymer sample admits some amount of compaction before fracture occurs, the composite has no real plateau region in its stress-strain curve. The post-mortem SEM reveals a narrow crack, locally tortuous as a result of matrix tearning but only a single unit cell wide. This crack likely propagated suddenly, when the failure strain of the architecture was reached.

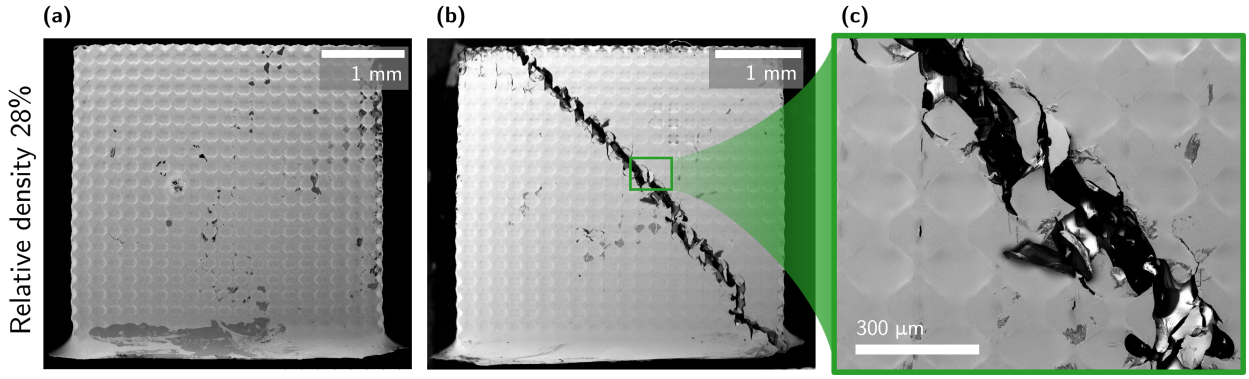

Figure 4.6: Scanning electron micrographs of a high relative density UpPhoto-PDMS composite before and after compression to fracture. The fracture pattern follows a shear band and the crack is only one unit cell wide, suggesting that the development of the crack was relatively sudden.

In the case of the polymer-SC61D system, experimental data reveals that all samples follow the stable compaction mode, independent of relative density. The SC61D compaction mode exhibits the same characteristics as the PDMS compaction mode; namely, the suppression of local instabilities due to matrix load transfer together with global deformation characterized by the progressive development of cracks. The stress-strain behavior was clearly dominated by the matrix material, particularly at high strains. Post-mortem SEM (Figure 4.7) reveals the presence of vertically oriented cracks at each unit cell which grow until they encounter each other, creating a macroscale crack that propagates vertically. In contrast to the PDMS composites, the SC61D composites are dominated by crush-band type cracks, as indicated by their vertical orientation.

Recalling from Chapter 3 that the polymer-SC61D system achieves the critical stiffness fraction, which is accompanied by increased load transfer capability across the matrix, the

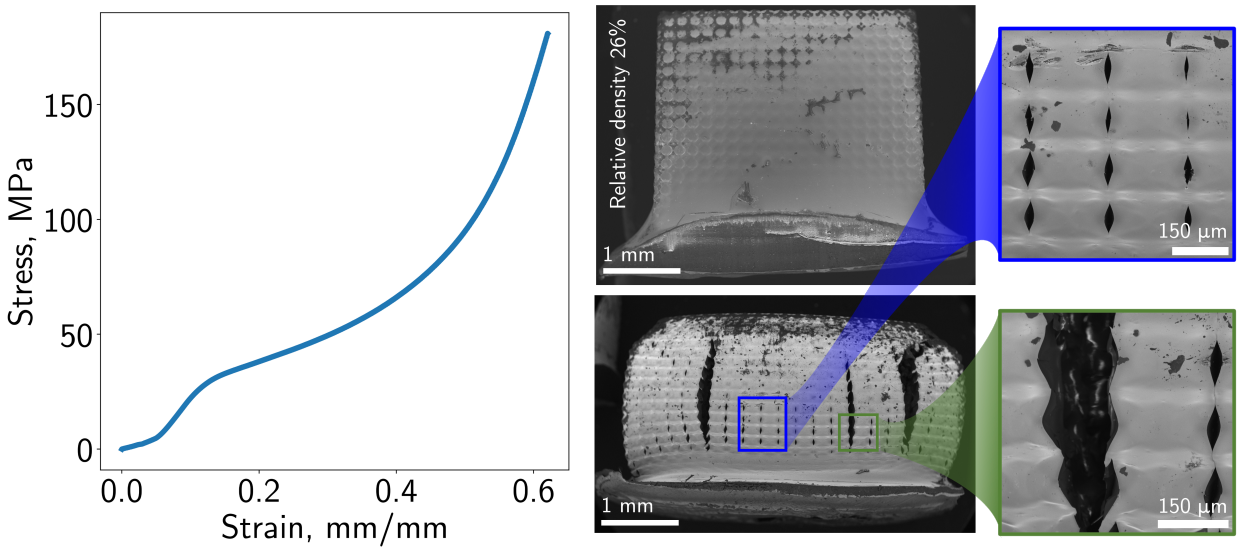

Figure 4.7: Stress-strain response and scanning electron micrographs of a typical UpPhoto-SC61D composite. These composites displayed compaction-type behavior independent of the relative density of the architecture, which was also characterized by vertically-oriented cracks nucleating from each unit cell.

uniformity of deformation behavior (i.e., independent of relative density) suggests that stiffening the matrix is one mechanism of changing the failure behavior in this composite system, for example if the stable compaction behavior is desired instead of fracture-dominated failure at higher relative densities.

4.2 Carbon system

We now turn to the mechanical behavior of the carbon-epoxy material system. As before, we will begin by benchmarking the composite performance using the performance of the architecture phase alone.

4.2.1 Single-material mechanical behavior

The behavior of the unfilled carbon Kelvin cell, depicted in Figure 4.8, was consistently observed in all samples, independent of the relative density (which ranged between 8% and 22%) or specimen size. In all cases, experiments reveal that the method of failure of the carbon Kelvin cell is dominated by layer-wise compaction. Unlike UpPhoto, pyrolyzed carbon is a brittle material that fails by fast fracture; as a result, the carbon Kelvin cell effectively experiences layer-wise fracture. It is seen that layers of unit cells fracture in a sequential manner from top to bottom (cf. Figure 4.8(b-e)). It is hypothesized that friction from the compression platen increases the magnitude of the local stress state at the topmost layer of unit cells, while the bulk of the specimen below the top layer remains unaffected. This crushing behavior thus begins at the top layer of unit cells and progresses downwards, layer-

by-layer, independent of the global strain of the specimen.

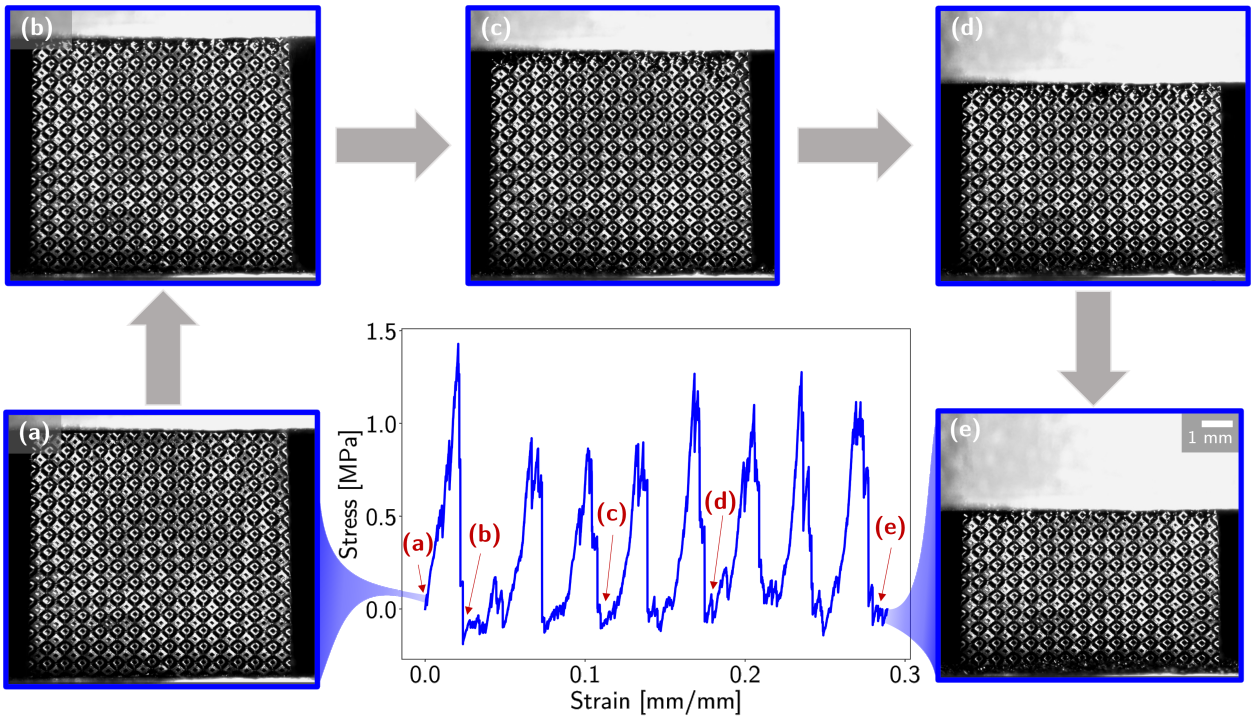

Figure 4.8: Uniaxial compressive behavior of the carbon Kelvin cell reinforcing phase. Upon application of load, the material is dominated by layer-wise compaction, and the brittle pyrolytic carbon leads to near-immediate fracture of beams. There is no observable local deformation mode; individual beams experience catastrophic fracture.

The stress-strain curve (Figure 4.8, center) reflects this layer-wise crushing behavior. It is characterized by a sawtooth pattern, approximately periodic. However, the major periodicity of the stress-strain curve does not match the number of unit cell layers, and post-test imaging reveals that an entire layer of unit cells does not fracture all at once. Rather, imperfections in the lattice locally nucleate failure within each layer, and failure proceeds in this local manner until an entire layer of unit cells is crushed. Damage to subsequent layers is also dependent on these imperfections, as the local character of damage in a given layer determines how stress is transferred to the next layer, and in turn dictates how the next layer fails. The local nature of this failure method is revealed in the stress-strain curve as a "high-frequency" oscillatory component, which appears to be superposed onto the lower-frequency sawtooth.

Moreover, it is seen that after the initial load peak is reached (corresponding to the failure of the topmost layer of unit cells in the pristine sample), the subsequent load peaks are all lower than the initial load peak. This further confirms the local nature of subsequent failure, as the sample never recovers to a point where an entire layer of unit cells is again able to simultaneously carry the load. Hence, the peak load is reached at a small value of strain, corresponding to the critical crushing strain of the first layer of unit cells. As a result, the load-carrying capacity of the carbon reinforcing phase is effectively determined only by a single layer of unit cells. This behavior is mechanically inefficient, but opens up many possibilities for harnessing the load-transfer capability of a composite structure.

4.2.2 Composite mechanical behavior

Shown in Figure 4.9 is the behavior of the carbon-epoxy composite Kelvin cell. The layer-wise compaction mechanism observed in the single-material architecture is entirely suppressed, and instead the composite experiences behavior similar to the stable compaction mechanism. Optical imaging of the compression tests reveal that the carbon composites develop a shear band (Figure 4.9(b)) just after the initial peak load is reached. The inset of Figure 4.9(b) shows that at the exterior of the specimen, the shear band is incredibly localized, affecting only one unit cell in each row. The unit cells within the shear band experience fracture together with local rotation, and this causes the two macroscopic halves of the specimen to tend to pull apart in the lateral direction.

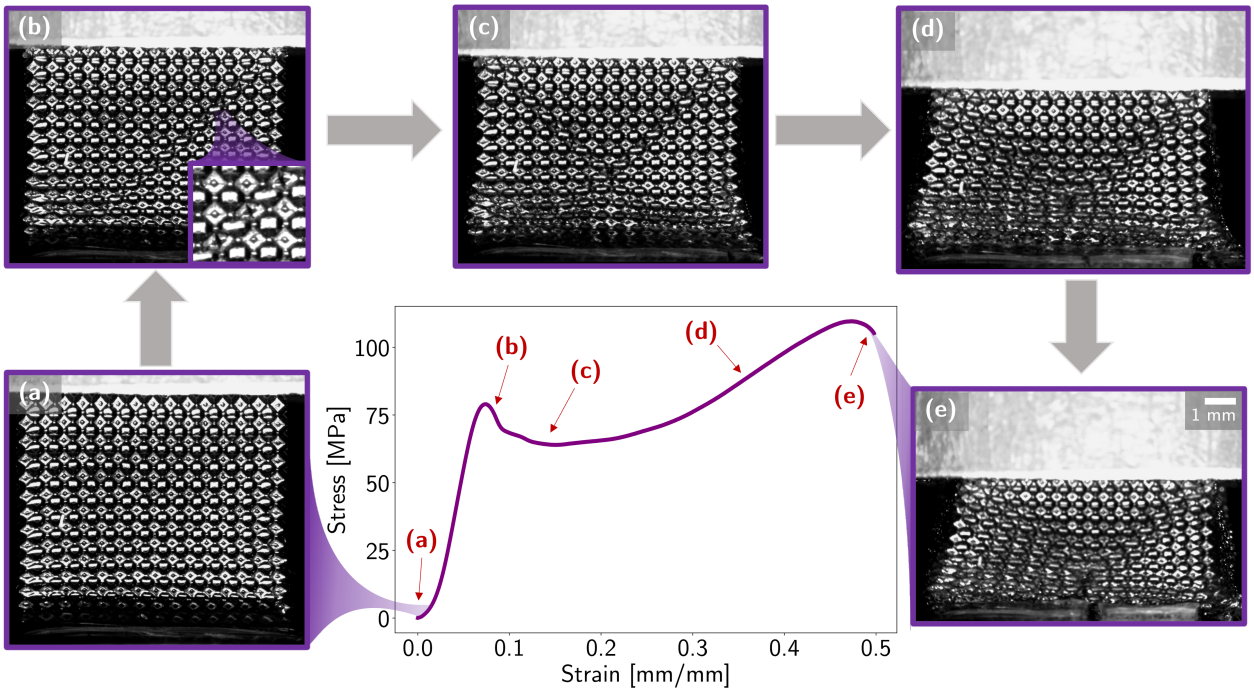

Figure 4.9: Uniaxial compressive behavior of the carbon-epoxy composite Kelvin cell (here, $\tilde{\rho} = 11.29\%$; this behavior was found to be independent of relative density). The composite is dominated by the development of primary (b) and secondary (c) shear bands, followed by crushing (d) and ultimate failure associated with a large-scale crack that tends to tear the specimen open (e).

Shortly after the development of the primary shear band, the load reaches a local minimum, and a secondary shear band (Figure 4.9(c)) develops in the specimen. This double-shear banding behavior was observed among all carbon-epoxy composite Kelvin cells regardless of relative density or specimen size, but the orientation of the primary and secondary shear bands (i.e., which diagonal served as the primary shear band) was arbitrary, likely dependent on imperfections in the fabrication process. The unit cells in the secondary shear band behave exactly as those in the primary shear band.

After the development of the secondary shear band, the measured load increases and the unit cell behavior is characterized by crushing in the unit cell rows underneath the two

shear bands (Figure 4.9(d)). At the same time, the unit cells above the shear bands remain undamaged. This crushing is characterized by a combination of compaction in the unit cells underneath the shear bands, together with lateral separation originating from the shear bands. Together, these effects drive the nucleation of a crack at the bottom compression platen which then spreads upwards as the specimen divides. When this crack has spread sufficiently, the load reaches an absolute maximum (Figure 4.9(e)), which typically occurs near a global strain of 50%. Following this global maximum load, the specimen experiences a dramatic drop of load followed by densification of the remainder of the specimen; for this reason, this load maximum was taken to coincide with the failure strain of the composite specimen.

4.2.3 Failure mode of the carbon composite system

The specimen images obtained during uniaxial compression testing (Figure 4.9) reveal the important mechanisms by which the carbon composite specimen fails. However, these optical images are restricted to the outside faces of the specimen. To obtain a proper three-dimensional characterization of specimen behavior during compression, we turned to X-ray computed tomography (XCT) to visualize the deformation behavior of the composite.

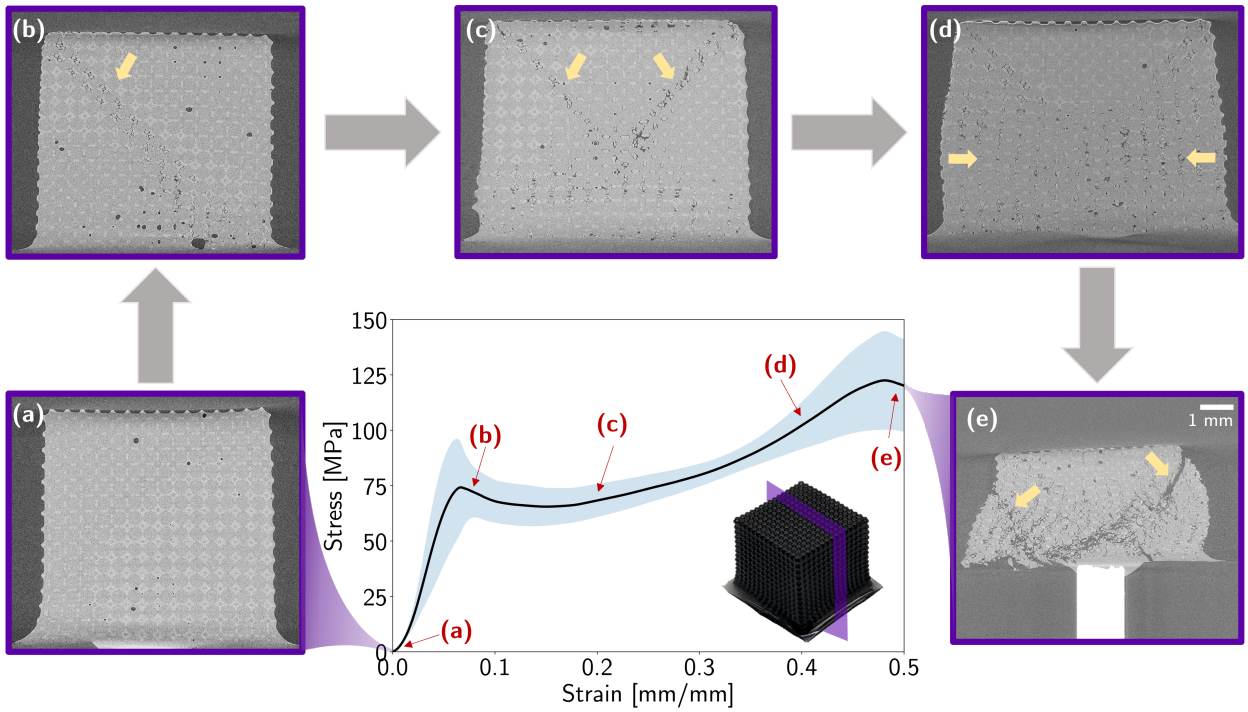

Figure 4.10: X-ray computed tomography reconstructions of carbon-epoxy composite specimens tested to various strains, each corresponding to the development of a critical stage of deformation.

To characterize the deformation behavior of the composite at various loading states, specimens of the same relative density were fabricated and tested to different strains, between the interval 0 and 50%. Figure 4.10 shows the result of these sequential XCT scans on

the cross-section indicated (we will refer to this orientation as "sagittal"); the corresponding points along an aggregate stress strain plot are marked. This stress-strain plot is an aggregate one because it represents the average stress-strain behavior of all specimens tested to a minimum of 50% global strain, across relative densities and specimen sizes. The shaded regions show a ± 1 standard deviation for this average. Importantly, although the stress values varied as a function of relative density, as expected, all specimens exhibited the same qualitative behavior as indicated by the shape of the stress-strain curve.

The salient features of the deformation response as seen in the optical images are reflected in the XCT scan reconstructions as well. In particular, the development of a primary shear band followed by a secondary shear band, then large-scale crushing of unit cells below the shear bands, followed by the propagation of a crack throughout the length of the specimen are seen. In Figure 4.10, these features are marked with yellow arrows for clarity.

One major benefit of the XCT reconstructions, past the verification of the characteristics observed in the optical images, is the ability to visualize the state of the specimen in three dimensions and from arbitrary orientations. Figure 4.11 shows the same sequence of reconstruction images, but featuring two cross-sections: sagittal (as before) and transverse.

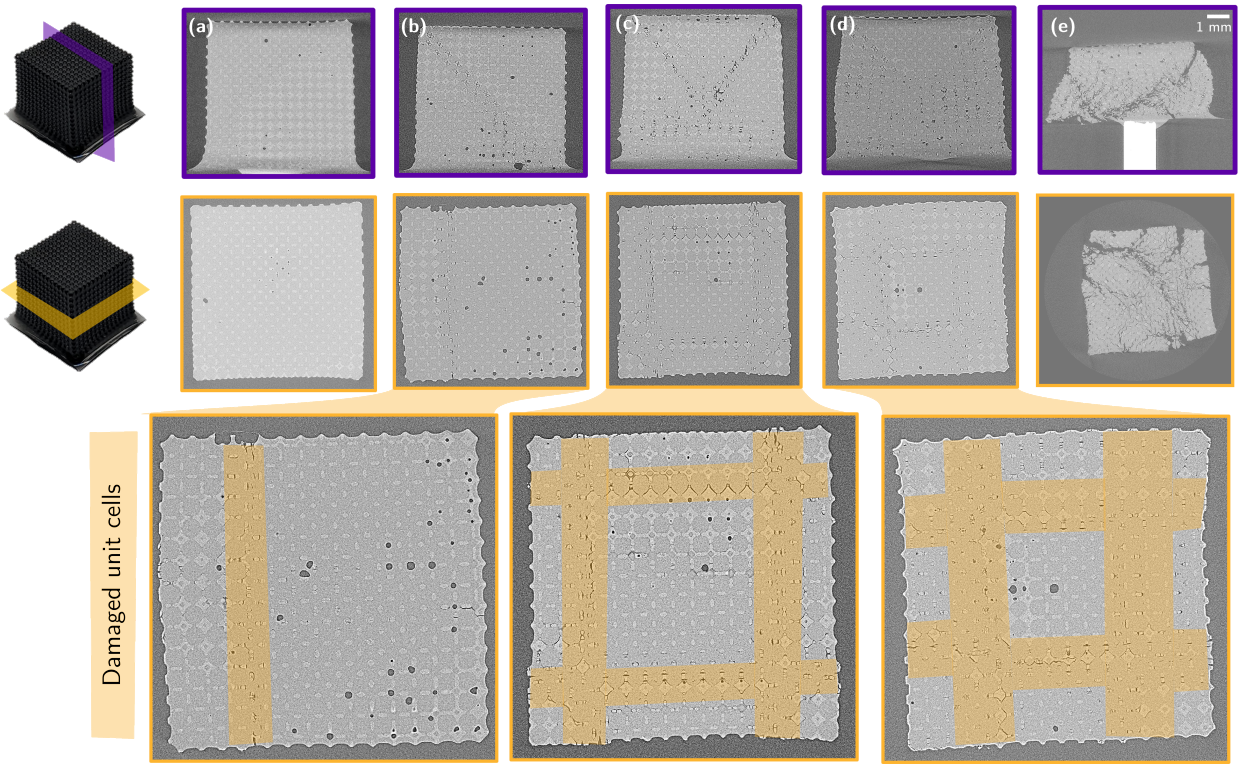

Figure 4.11: Sagittal (top row) and transverse (bottom row) cross-sections of carbon-epoxy composites tested to the strain values indicated on Figure 4.10. Two section views together enable the visualization of deformation features across three dimensions. The transverse views clearly demonstrate how the extent of damage to unit cells (highlighted in yellow) evolves with increasing macroscopic deformation.

Taken together, these perpendicular cross-sections reveal important aspects of the failure mechanisms that is not available in the optical view. In particular, it is seen from 4.11(b)

that the primary shear band spans the depth of the specimen but is localized in the lateral dimension, affecting only one row of unit cells. This offers one explanation as to why the emergence of a shear band does not lead to catastrophic failure. Figure 4.11(c) reveals that the secondary shear bands are symmetric in nature; moreover, secondary shear bands are also created on the transverse plane. This results in a "ring" of fractured unit cells, outside of which and within are pristine unit cells. As the deformation progresses into the crushing regime and the number of affected unit cells grows, Figure 4.11(d), an inner ring remains pristine, again offering an explanation for the lack of loss in load capacity despite clear widespread fracture.

Moreover, we can see from Figure 4.11(e) that the through-specimen crack takes a tortuous route through the specimen in all three dimensions, finding a serpentine path among unit cells. As discussed before, the increased path length associated with this final crack is another contribution to the increased strain energy associated with failure of the composite specimen. A promising future endeavor is to use image analysis software to numerically compute the path length of each crack as it evolves, connecting crack growth to energy dissipation, deformation behavior, and the global stress-strain response.

Finally, the XCT reconstructions also reveal that cracks do not originate from the small voids (resulting from the fabrication process, totaling less than 1% of total specimen volume) observed in the undeformed specimens (as visible in 4.11(a)). Moreover, neither the shear-band regions nor the compaction regions appear to be affected the presence of voids, suggesting that their role as stress concentrators can be neglected. This result confirms that the facile fabrication method developed for these architected composites yields robust material samples with a high degree of tolerance for such small imperfections.

4.2.4 The interaction effect

Having examined the behavior of the single-material and composite Kelvin cells in a qualitative fashion, and seeing a drastic difference in the nature of their deformation, we now turn toward quantifying the effect of the composite infill process on material properties. Figure 4.12 shows the stress-strain behavior of an unfilled carbon Kelvin specimen (blue curve), plotted to the peak load, as well as the stress-strain behavior of the monolithic epoxy resin (red curve), normalized by mass according to the measured relative density of the reinforcing phase. The orange curve represents a simple linear superposition of the two component stress-strain curves, and serves as an estimate of the composite material properties. Because the unfilled architecture curve is effectively normalized by mass, and the epoxy resin curve is normalized by mass, the orange superposition curve represents a mass-normalized estimate of the composite properties.

The green curve in Figure 4.12 shows the actual behavior of a composite specimen with the same relative density (i.e., the same total mass as the two parts represented by the orange curve). Clearly, the composite outperforms the superposition estimate in terms of load capacity (stress sustained at a given amount of global strain), leading to a higher Young's modulus and a higher toughness to a given strain. Importantly, this trend was observed in all carbon composite specimens, independent of relative density. This concept has been noted before in the composites literature [53, 54], where it is called the "interaction effect". The interaction effect represents an enhancement of mechanical performance unique to and due

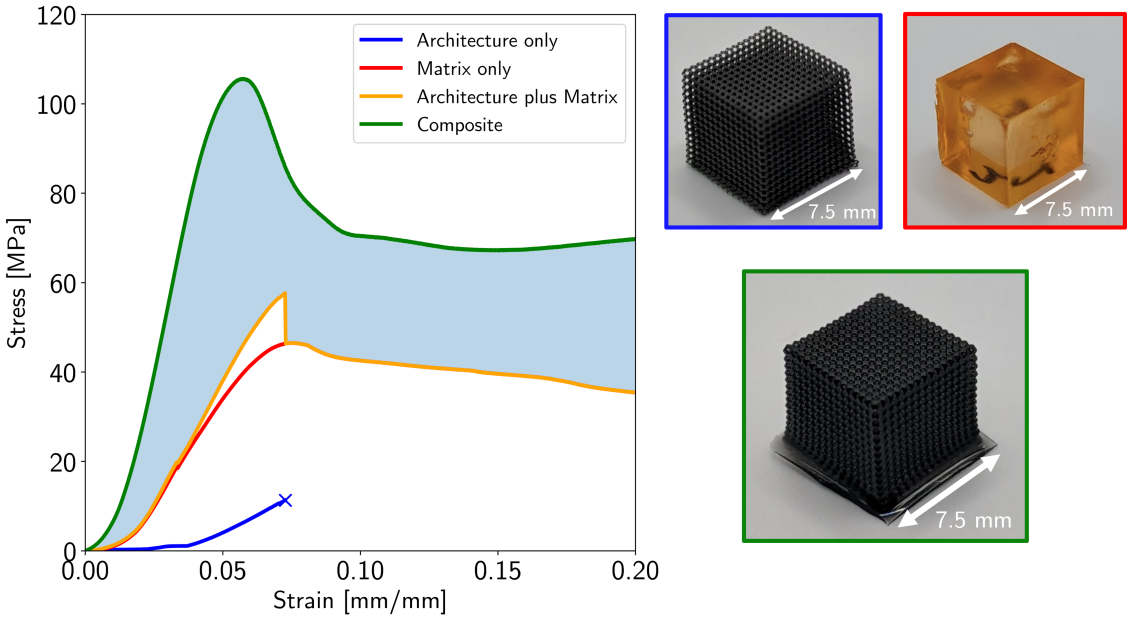

Figure 4.12: Constructing the interaction effect (blue shaded region): superposition of the individual stress-strain curves for the architecture (blue) and matrix phases (red) yields a mass-normalized estimate (orange) of the composite behavior, which is found to be globally lower than the actual composite behavior (green) by an amount called the interaction effect.

to the nature of the composite, quantifying by exactly how much the composite exceeds the sum of its parts.

In our case, the interaction effect is the result of the favorable load distribution in the composite, resulting in a stark contrast in deformation behavior with the layer-wise failure mechanism of the unfilled specimen. In particular, the increase in stiffness can be attributed to the entire height of the composite working together to sustain the applied loading. The increase in toughness can be attributed to the damage-tolerant mechanism of load transfer in the composite system. Even though failure begins to occur at a low value of the global strain, it is confined to the shear bands, and the remainder of the specimen is able to take up the remaining load. This pathway for subsequent failure delocalization is a critical method of maximizing load capacity in the composite. Finally, the presence of the matrix phase itself, combined with the geometric tortuosity provided by the architecture, delays the propagation of a critically-sized crack through the specimen, increasing the amount of energy dissipated during the fracture process.

The interaction effect can be observed in the polymer-based system, as well (Figure 4.13). It is seen that for samples undergoing the stable compaction behavior (i.e., low relative-density UpPhoto/PDMS composites and all UpPhoto/SC61D composites) that a net positive interaction effect is obtained, demonstrating that the enhancement of stiffness and toughness is obtained independent of material system. Instead, it is primarily attributable to mechanical behavior; namely, the development of a stable compaction mechanism leads easily to a pathway for a significant increase in load capacity.

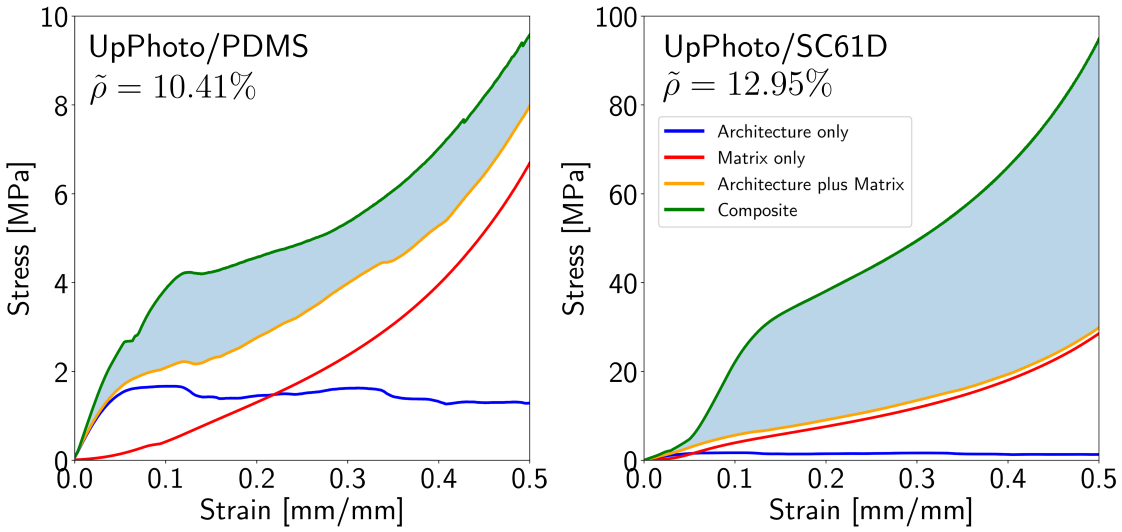

Figure 4.13: Interaction effect for the polymer system: composites of UpPhoto with both matrix materials demonstrated a net increase in stiffness and toughness over the sum of their constituent parts.

4.3 Discussion

A simple integration of the experimental stress-strain curves suggests that the toughness (i.e., the volumetric energy absorption capacity) of our carbon-epoxy composites to a strain of 50% is 50.99 ± 6.11 MJ m^{-3}. With a typical density of 1.2 g cm^{-3} as fabricated, this yields an average specific energy absorption (SEA) of 42.49 ± 5.09 J g^{-1}. Figure 4.14 plots this figure on an Ashby plot of energy absorption capacity versus material density, along with a variety of other single-material and composite architected materials found throughout the literature [55, 56, 57, 58, 19, 59, 60, 61, 62, 63]. If not explicitly stated in each reference, the energy absorption capacity was calculated using published stress-strain data to ultimate failure or to 50% strain, whichever came first.

With reference to this plot, it can be seen that in general, architected materials made using metallic precursors generally have a high density, due to the density of bulk metal. However, metallic metamaterials can attain high ultimate strains and in doing so, high energy absorption capacities. On the other hand, carbon-based materials vary in density across orders of magnitude primarily due to differences in morphology (e.g., carbon nanotube-based systems are much less dense than plate-based carbon lattices), with a corresponding variation in energy absorption capacity. There are few examples of architected materials based on polymers that can attain high energy absorption capacities, with one notable structure being that of Kumar et al. [59], which attains an SEA value close to the monolithic resin used in our experiments. Finally, the plot offers an alternative visualization of the interaction effect. Because of its low failure strain, the contribution of toughness due to the carbon phase alone is negligibly small compared to the matrix phase alone (on average, 0.08 MPa versus 30.98 MPa), so the interaction effect can be viewed as the difference between the monolithic resin (SEA $= 25.82 \pm 0.39$ J g^{-1}) and the composite. In terms of specific energy absorption, the

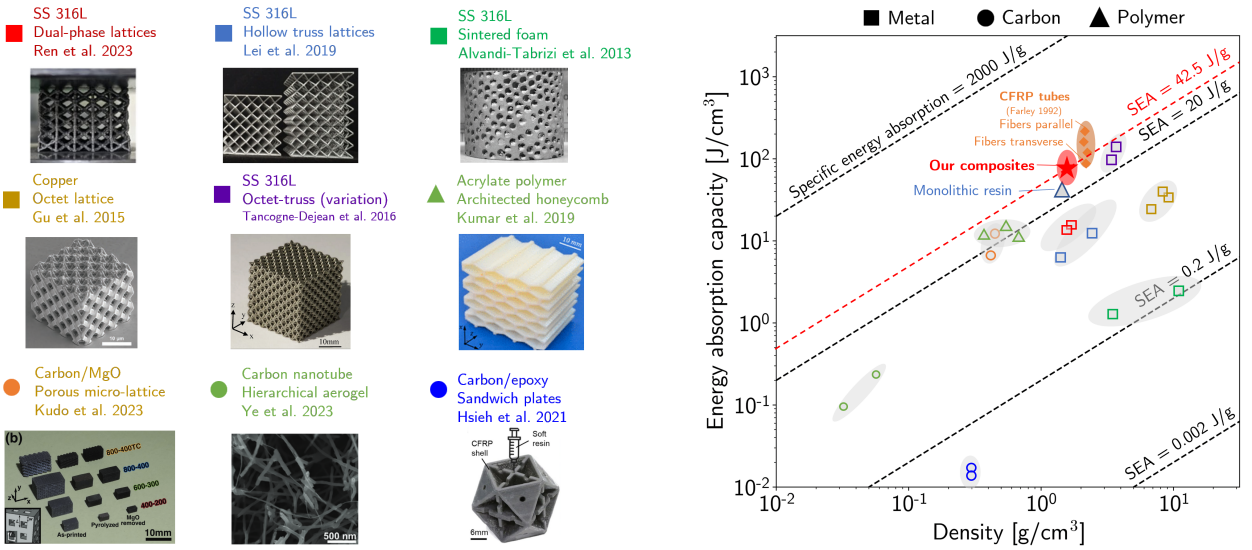

Figure 4.14: Ashby plot of energy absorption capacity versus density for several single-material and composite 3D-architected materials representing the current state-of-the-art [55, 56, 57, 58, 19, 59, 60, 61, 62, 63]. Also plotted is data for the monolithic epoxy resin used in this study, and wound carbon fiber reinforced polymer (CFRP) tubes tested in various orientations relative to their winding direction [63].

composites in this study thus provide, on average, a 97.48% increase over the sum of their constituent components.

Moreover, our composites have a specific energy absorption greater than all of the architected examples shown. Of note in particular, our composites, being orthotropic, outperform some CFRP tubes fabricated by winding of fibers [63]. These CFRP tubes are highly anisotropic and weakest when loaded transverse to the fiber orientation. However, CFRP tubes with the majority of fibers aligned to the loading direction attain a higher specific energy absorption than our architected composites, as expected. This suggests that three-dimensional architected composites may realistically be used in applications currently served by CFRP tubes, but where the flexibility afforded by freeform fabrication offers a unique advantage.

Chapter 5

Architecting a stress state

Having thoroughly considered the behavior of the composite Kelvin cell, a geometry that has been well-studied in the literature, we now have a basic understanding of the properties of architected composite materials. We know that the matrix and architecture phases work together to distribute the applied load, leading to delocalization of stress and an increase in the tortuosity of cracks after a critical strain is reached. The result is an enhancement of stiffness and toughness in the composite, which we have called the interaction effect.

We now turn to the question of *architecting* the stress state, and correspondingly the compressive behavior of, a composite material. We accomplish this using a careful selection of both geometry and constituent material.

5.1 A thought experiment

Consider the two unit cells shown in figure 5.1. The unit cell in Figure 5.1(a) fails to satisfy the Maxwell criterion and is therefore bending-dominated. It is straightforward to see that a uniaxial compression in the vertical direction would tend to cause the other beams to push outward, as in the Kelvin cell. Indeed, simulations suggest that the effective Poisson ratio (defined to be the negative of the ratio of lateral strain to longitudinal strain in the limit of small strains) of the unit cell in Figure 5.1(a) is $\tilde{\nu} = 0.47$.

The unit cell in Figure 5.1(b) has the same relative density (namely, 10%) as the unit cell in Figure 5.1(a); to this end, it simply represents a redistribution of the same amount of mass. (To achieve the same relative density in a different geometrical configuration, the average beam diameter is slightly smaller in the unit cell of Figure 5.1(b) than of Figure 5.1(a)). Moreover, the unit cell in Figure 5.1(b) also fails to satisfy the Maxwell criterion.

Motivated by the traditional notion of bending and stretching in architected materials, the behavior of these two unit cells would be classified identically in the traditional sense. In particular, they are both bending-dominated. However, unlike the unit cell in Figure 5.1(a), the unit cell in figure 5.1(b) is *auxetic*: as the unit cell is compressed longitudinally, the lateral beams tend to be pushed *inwards* and the effective Poisson ratio of this unit cell is negative, $\tilde{\nu} = -0.23$. Figure 5.2 shows the result of finite element simulations that confirm the auxetic nature of this unit cell. For simplicity, we will henceforth refer to the unit cell in Figure 5.1(a) as the "ordinary" geometry, and the unit cell in Figure 5.1(b) as the "auxetic"

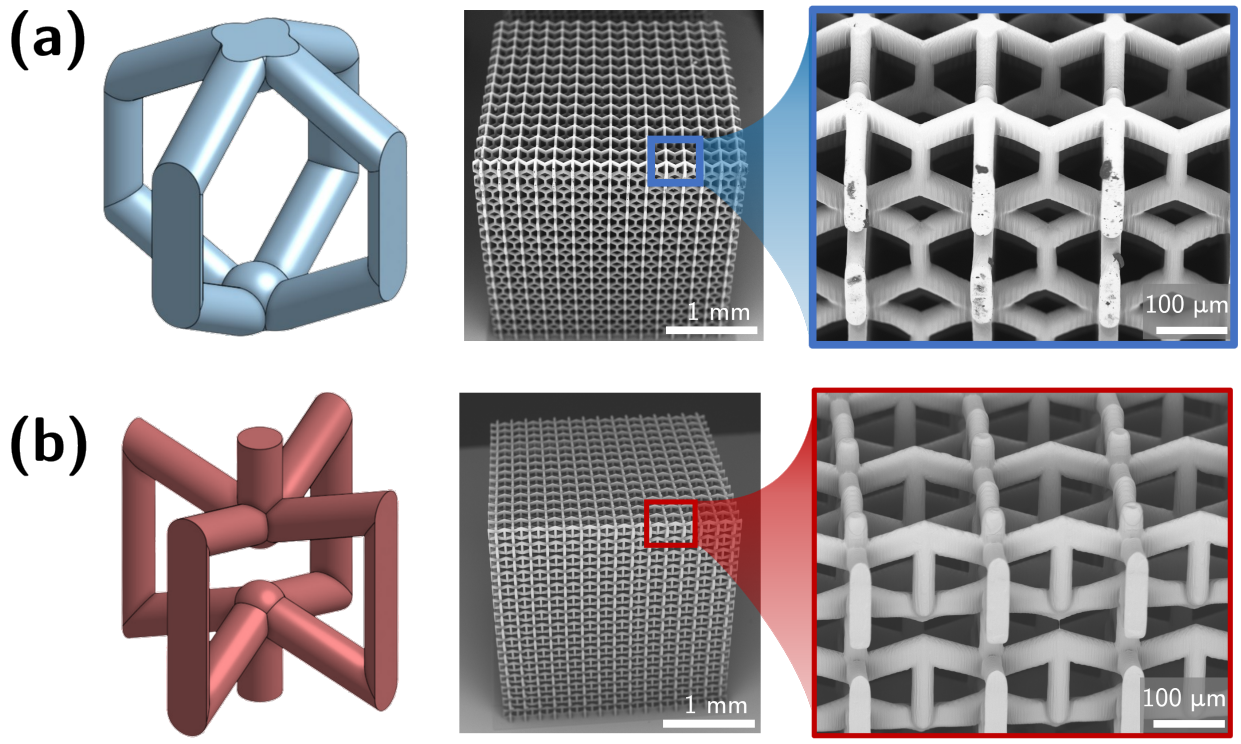

Figure 5.1: CAD models and fabricated tessellations of two unit cells having the same relative density, which both fail to satisfy the Maxwell criterion. The unit cell in (a) has a positive Poisson ratio, whereas the unit cell in (b) has a negative Poisson ratio.

geometry.

We have seen in our investigations of the polymer-based Kelvin system that the matrix material PDMS is nearly incompressible. An incompressible material can sustain an arbitrary hydrostatic pressure without deformation; moreover, a given deformed configuration of an incompressible material can sustain an arbitrary hydrostatic pressure in addition to the stress needed to cause the deformation. The thought experiment is: suppose we created composites with the auxetic unit cell infiltrated with PDMS. If the auxetic unit cell wants to deform to a state whereby the enclosed volume is smaller than the reference configuration, but the PDMS is nearly incompressible, how will this affect the stress state in the composite? Specifically, if we are able to create a "pocket" of hydrostatic stress in the matrix material, can this lead to increased macroscopic load capacity of the material?

5.2 Fabrication

To investigate this proposed mechanism of strengthening, $15 \times 15 \times 15$ tessellations of both the ordinary and auxetic unit cells were fabricated using TPL as shown in Figure 5.1. The TPL method was chosen primarily because between the two fabrication methods, it had the best spatial resolution and thus most preserved the fidelity of critical features. In particular, simulation results suggest that the Poisson ratio of the auxetic unit cell is highly dependent on the orientation and dimension of the beams, so TPL provided the best pathway to correlate

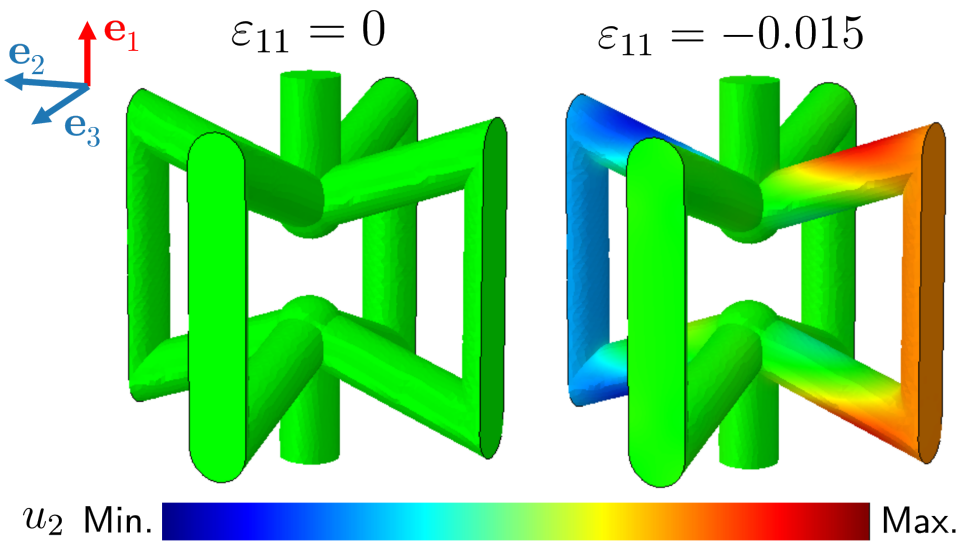

Figure 5.2: Simulated response of the auxetic unit cell to a small vertical compressive displacement. The lateral edges of the unit cell contract towards the middle of the unit cell, giving rise to a negative Poisson ratio.

experimental and simulation results for this initial validation. After printing, the unit cells were infiltrated with PDMS in the manner described in Chapter 2. We then tested unfilled samples (i.e., the reinforcing phase alone) and composite samples of both geometries in uniaxial compression.

5.3 Discussion

Figure 5.3 shows the stress-strain curves of the two single-material (architecture and matrix) phases, their sum, and the stress-strain curve of the composite in the same way as presented before for the Kelvin geometry. The interaction effect is again shaded in blue.

In the single-material case, the ordinary geometry outperforms the auxetic geometry in terms of stiffness and toughness. Past the elastic regime, it was observed that the single-material auxetic unit cell tended to collapse by buckling once a critical strain was reached. Specifically, the vertically oriented beams connecting unit cells in the direction of compression carried the entire load and hence first reached a critical buckling load. Conversely, the single-material ordinary unit cell behaved in a much more stable manner, with load drops corresponding to local failure being stabilized by additional unit cells. In the high-strain limit, both unit cells behaved like the compaction-dominated Kelvin cell, with a stress-strain response characterized by a plateau stress until the densification regime was reached.

Measured to 20%, which was before the onset of global failure in either composite, a modest but non-zero interaction effect (35.6% increase in toughness and 24.5% increase in Young's modulus) was measured for the ordinary unit cell. However, the interaction effect measured for the auxetic unit cell was dramatically higher (171.3% increase in toughness and 158.8% increase in Young's modulus), as predicted. Moreover, the composite auxetic cell

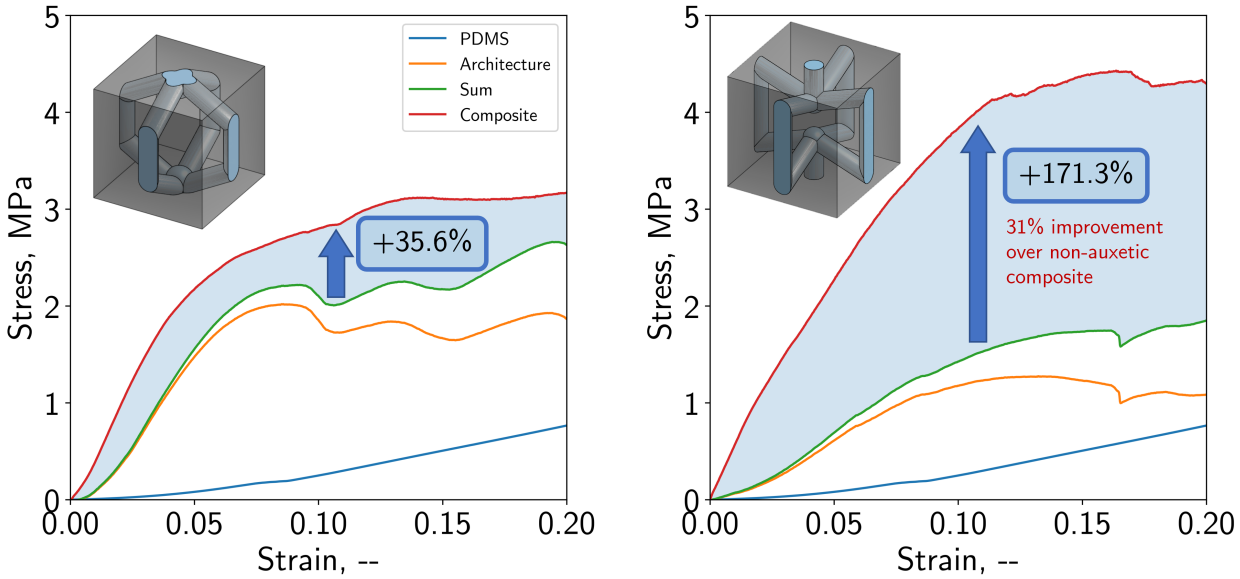

Figure 5.3: Experimentally determined stress-strain curves for the single-material reinforcing phase, the monolithic matrix (PDMS), and the architected composite in the case of the ordinary (left) and auxetic (right) unit cells. Upon infiltration, both geometries exhibit an increase in stiffness and toughness, but the relative increase is significantly higher in the case of the auxetic cell.

showed a higher load capacity than the composite ordinary cell (i.e., the sustained load at a given macroscopic strain was higher for all strains). Quantitatively, the toughness (to 20% macroscopic strain) was 31% higher in the case of the composite auxetic unit cell compared to the composite ordinary cell. This behavior is opposite of the trends observed in the single-material case, where the ordinary cell was both stiffer and tougher than the auxetic cell.

At high strains, both composite specimens demonstrated matrix-dominated behavior with stresses increasing rapidly. Both composites sustained higher stresses than the sample of pure PDMS. However, the auxetic unit cell exhibited an even higher stress than the ordinary cell even in this high-strain regime. This demonstrates the sustained effect of the quasi-hydrostatic stress state developed in the matrix material, proving a stable interaction effect at high strains.

An explanation for the enhancement in load capacity for the auxetic system, and a confirmation of our hypothesis about hydrostatic pressure, is obtained using finite element analysis (Figure 5.4). A simulation of the UpPhoto-PDMS system, modeling the PDMS as an incompressible Arruda-Boyce polymer using constants fit from experimental data, shows an increased state of mean normal pressure in the composite auxetic cell. As a result of the periodic boundary conditions enforced on the simulated cell, reflecting the high number of unit cells in the fabricated tessellation, the mean normal pressure $\bar{p}$ is elevated everywhere in the matrix material, not just "inside" the pocket created by architecture. This effect is explained by the tendency of the auxetic structure to collapse onto itself, pulling its neighbors inward and creating additional regions of increased hydrostatic pressure in the space between

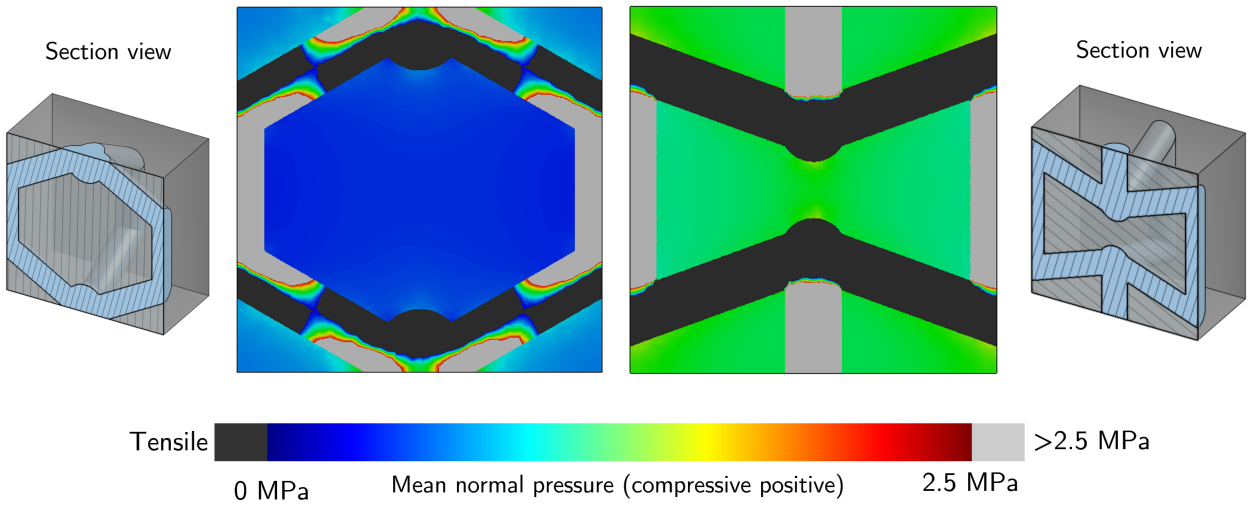

Figure 5.4: Finite element simulation of the ordinary (left) and auxetic (right) unit cells filled with an incompressible matrix (material properties taken from experimental PDMS data) at a unit cell strain of 3%. A plot of the mean normal pressure in the cross section of each composite unit cell reveals a higher mean normal pressure in the auxetic cell, giving rise to the increased interaction effect.

unit cells. A consequence of this is that the beams of the architecture transition into a stretching state, despite a sub-critical stiffness fraction (here, $E_m/E_f = 1.54 \times 10^{-3}$). This suggests the possibility of another pathway by which a stretching-dominated response can be observed in a bending-dominated geometry. Moreover, both specimens exhibited an increase in the mean normal pressure over a simulation of monolithic PDMS, which experiences a uniform value $\bar{p} = 0.061$ MPa at the same strain. This result again confirms that the matrix and architecture phases work together to achieve an increase in load-carrying capacity, and reinforces the importance of architecture in the design of such a composite.

Chapter 6

Summary and outlook

6.1 Summary

In this work, we have considered the mechanical behavior of two systems of architected interpenetrating phase composite materials. We consider a polymer-polymer system that takes advantage of high-resolution digital fabrication to achieve precise geometrical control with a high degree of repeatibility, and a carbon-polymer system that attains mechanical properties comparable to existing examples of architected materials made from various materials.

In the elastic regime, we see that independent of material system, there exists a critical balance of material parameters that dictates the stretching- or bending-dominated behavior of the architecture. In particular, with a critical stiffness fraction, we can create a stretching-dominated response in an architecture that fails to satisfy Maxwell's criterion, challenging traditional notions linking geometry to mechanical behavior. We see that when the matrix is sufficiently stiff, a stress transfer pathway develops within the matrix phase that acts like the missing kinematic connections in the geometry.

Past the elastic regime, the matrix continues to redistribute applied stresses throughout the specimen, delocalizing load away from compaction bands, meaning that the entire specimen cooperates to carry the load. This results in increased energy dissipation and a higher load capacity in the composite compared to the sum of its constitutent materials. Finally, even when the specimen begins to fail by shear banding, the load sustained by the composite continues to increase, because any cracking in the specimen is redirected along a tortuous path. These phenomena combine to create an "interaction effect" contributing to high toughness and high stiffness values, in particular outperforming the addition of the single-phase constituents at the same amount of mass.

Finally, we see that architectural design offers a pathway to tune the stress state in, and subsequent response of, a composite materials. As a simple demonstration of this concept, we create a material system having auxetic character in its architecture, infilled with a matrix that is nearly incompressible. We see that compared to the behavior of the architecture alone, the addition of a matrix material dramatically strengthens the auxetic unit cell, contributing to an interaction effect that eventually even outperforms a non-auxetic geometry.

6.2 Future work and outlook

The opportunities for tuning the mechanical performance of three-dimensional composites is made vast by the near-endless potential of architectural design. In particular, the structural enhancements afforded by novel architectural designs like shell-based or plate-based lattices, or even aperiodic structures, can be harnessed to change how damage initiates and propagates through a composite. Moreover, novel approaches like the application of crystal strengthening mechanisms to architected materials [64, 65] hold tremendous potential when combined with the framework of interpenetrating phase composites. The influence of architected disorder and the control of bending and stretching through this framework [66] is another potential avenue towards developing resilient and damage-tolerant composites using architecture.

Finally, the fabrication and characterization techniques developed here can be extended to deepen our understanding of how these and virtually any other three-dimensional architected composites behave. In particular, the pyrolysis process can be used to create other high-strength materials like fused silica glass, metals, or technical ceramics. In turn, these reinforcing phases can be infiltrated with nearly any matrix material to create a diverse range of composites with varied, highly-tunable mechanical properties. With the help of optical imaging, XCT reconstructions, and advanced image processing capabilities, it will be possible to intimately understand how architectural design, constituent material choice, and their interaction contribute to mechanical performance. This represents a critical first step in the design and subsequent optimization of stiff, strong, and robust architected composite materials.

References

[1] Michael F. Ashby. "Material Property Charts". In: *Materials Selection in Mechanical Design*. Elsevier, 2011, pp. 57–96. ISBN: 9781856176637. DOI: 10.1016/b978-1-85617-663-7.00004-7. URL: http://dx.doi.org/10.1016/B978-1-85617-663-7.00004-7.

[2] Xuan Zhang, Yujia Wang, Bin Ding, and Xiaoyan Li. "Design, Fabrication, and Mechanics of 3D Micro-/Nanolattices". In: *Small* 16.15 (Sept. 2019). ISSN: 1613-6829. DOI: 10.1002/smll.201902842. URL: http://dx.doi.org/10.1002/smll.201902842.

[3] Cameron Crook, Jens Bauer, Anna Guell Izard, Cristine Santos de Oliveira, Juliana Martins de Souza e Silva, Jonathan B Berger, and Lorenzo Valdevit. "Plate-nanolattices at the theoretical limit of stiffness and strength". In: *Nature Communications* 11.1 (Dec. 2020), p. 1579. ISSN: 2041-1723. DOI: 10.1038/s41467-020-15434-2. URL: http://dx.doi.org/10.1038/s41467-020-15434-2%20http://www.nature.com/articles/s41467-020-15434-2.

[4] N. A. Fleck, V. S. Deshpande, and M. F. Ashby. "Micro-architectured materials: past, present and future". In: *Proceedings of the Royal Society A: Mathematical, Physical and Engineering Sciences* 466.2121 (June 2010), pp. 2495–2516. ISSN: 1471-2946. DOI: 10.1098/rspa.2010.0215. URL: http://dx.doi.org/10.1098/rspa.2010.0215.

[5] Sebastian Krodel, Tommaso Delpero, Andrea Bergamini, Paolo Ermanni, and Dennis M. Kochmann. "3D auxetic microlattices with independently controllable acoustic band gaps and quasi-static elastic moduli". In: *Advanced Engineering Materials* 16.4 (2014), pp. 357–363. ISSN: 15272648. DOI: 10.1002/adem.201300264.

[6] Lei Zhang, Stefanie Feih, Stephen Daynes, Shuai Chang, Michael Yu Wang, Jun Wei, and Wen Feng Lu. "Energy absorption characteristics of metallic triply periodic minimal surface sheet structures under compressive loading". In: *Additive Manufacturing* 23.August (Oct. 2018), pp. 505–515. ISSN: 22148604. DOI: 10.1016/j.addma.2018.08.007. URL: https://linkinghub.elsevier.com/retrieve/pii/S2214860418304688.

[7] Julia R. Greer and Vikram S. Deshpande. "Three-dimensional architected materials and structures: Design, fabrication, and mechanical behavior". In: *MRS Bulletin* 44.10 (Oct. 2019), pp. 750–757. ISSN: 1938-1425. DOI: 10.1557/mrs.2019.232. URL: http://dx.doi.org/10.1557/mrs.2019.232.

[8] Jens Bauer, Lucas R. Meza, Tobias A. Schaedler, Ruth Schwaiger, Xiaoyu Zheng, and Lorenzo Valdevit. "Nanolattices: An Emerging Class of Mechanical Metamaterials". In: *Advanced Materials* 29.40 (Sept. 2017). ISSN: 1521-4095. DOI: 10.1002/adma.201701850. URL: http://dx.doi.org/10.1002/adma.201701850.

[9] Lauren C. Montemayor, Lucas R. Meza, and Julia R. Greer. "Design and Fabrication of Hollow Rigid Nanolattices via Two-Photon Lithography". In: *Advanced Engineering Materials* 16.2 (Oct. 2013), pp. 184–189. ISSN: 1527-2648. DOI: 10.1002/adem.201300254. URL: http://dx.doi.org/10.1002/adem.201300254.

[10] Vikram S. Deshpande, M. F. Ashby, and Norman A. Fleck. "Foam topology: Bending versus stretching dominated architectures". In: *Acta Materialia* 49.6 (2001), pp. 1035–1040. ISSN: 13596454. DOI: 10.1016/S1359-6454(00)00379-7.

[11] Norman A. Fleck. "An overview of the mechanical properties of foams and periodic lattice materials". In: *Cellular Metals and Polymers 2004* 8585858585 (2004), pp. 1–4.

[12] M. F. Ashby. "The properties of foams and lattices." In: *Philosophical transactions. Series A, Mathematical, physical, and engineering sciences* 364.1838 (2006), pp. 15–30. ISSN: 1364-503X. DOI: 10.1098/rsta.2005.1678. URL: http://rsta.royalsocietypublishing.org/cgi/doi/10.1098/rsta.2005.1678.

[13] Lorna J. Gibson and Michael F. Ashby. *Cellular Solids: Structure and Properties*. 2nd ed. Cambridge: Cambridge University Press, 1999. ISBN: 978-0521499118. URL: https://doi.org/10.1017/CBO9781139878326.

[14] S. Pellegrino and C. R. Calladine. "Matrix Analysis of Statically and Kinematically Indeternimate Frameworks". In: *International Journal of Solids and Structures* 22.4 (1986), pp. 409–428.

[15] Denis Weaire. "Kelvin's ideal foam structure". In: *Journal of Physics: Conference Series* 158 (Apr. 2009), p. 012005. DOI: 10.1088/1742-6596/158/1/012005. URL: https://doi.org/10.1088/1742-6596/158/1/012005.

[16] Lucas R. Meza, Gregory P. Phlipot, Carlos M. Portela, Alessandro Maggi, Lauren C. Montemayor, Andre Comella, Dennis M. Kochmann, and Julia R. Greer. "Reexamining the mechanical property space of three-dimensional lattice architectures". In: *Acta Materialia* 140 (Nov. 2017), pp. 424–432. ISSN: 13596454. DOI: 10.1016/j.actamat.2017.08.052. URL: http://dx.doi.org/10.1016/j.actamat.2017.08.052%20https://linkinghub.elsevier.com/retrieve/pii/S1359645417307073.

[17] Andrew Y. Chen, Ailin Chen, Andrew Fitzhugh, Aja Hartman, Pierre Kaiser, Ihuoma Nwaogwugwu, Jun Zeng, and Grace X. Gu. "Multi Jet Fusion printed lattice materials: characterization and prediction of mechanical performance". In: *Materials Advances* 4.4 (2023), pp. 1030–1040. ISSN: 2633-5409. DOI: 10.1039/d2ma00972b. URL: http://dx.doi.org/10.1039/D2MA00972B.

[18] Carlos M Portela, Julia R Greer, and Dennis M Kochmann. "Impact of node geometry on the effective stiffness of non-slender three-dimensional truss lattice architectures". In: *Extreme Mechanics Letters* 22 (July 2018), pp. 138–148. ISSN: 23524316. DOI: 10.1016/j.eml.2018.06.004. URL: https://doi.org/10.1016/j.eml.2018.06.004%20https://linkinghub.elsevier.com/retrieve/pii/S2352431618300725.

[19] Thomas Tancogne-Dejean, Adriaan B. Spierings, and Dirk Mohr. "Additively-manufactured metallic micro-lattice materials for high specific energy absorption under static and dynamic loading". In: *Acta Materialia* 116 (2016), pp. 14–28. ISSN: 13596454. DOI: 10.1016/j.actamat.2016.05.054. URL: http://linkinghub.elsevier.com/retrieve/pii/S1359645416304153.

[20] Lucas R. Meza, Satyajit Das, and Julia R. Greer. "Strong, lightweight, and recoverable three-dimensional ceramic nanolattices". In: *Science* 345.6202 (Sept. 2014), pp. 1322–1326. ISSN: 0036-8075. DOI: 10.1126/science.1255908. URL: http://www.sciencemag.org/cgi/doi/10.1126/science.1255908.

[21] Oraib Al-Ketan, Rachid Rezgui, Reza Rowshan, Huifeng Du, Nicholas X. Fang, and Rashid K. Abu Al-Rub. "Microarchitected Stretching-Dominated Mechanical Metamaterials with Minimal Surface Topologies". In: *Advanced Engineering Materials* 20.9 (Sept. 2018), p. 1800029. ISSN: 14381656. DOI: 10.1002/adem.201800029. URL: http://doi.wiley.com/10.1002/adem.201800029.

[22] Thomas Tancogne-Dejean, Marianna Diamantopoulou, Maysam B. Gorji, Colin Bonatti, and Dirk Mohr. "3D Plate-Lattices: An Emerging Class of Low-Density Metamaterial Exhibiting Optimal Isotropic Stiffness". In: *Advanced Materials* 30.45 (Nov. 2018), p. 1803334. ISSN: 09359648. DOI: 10.1002/adma.201803334. URL: http://doi.wiley.com/10.1002/adma.201803334.

[23] Xiaoyu Zheng et al. "Ultralight, Ultrastiff Mechanical Metamaterials". In: *Science* 344.6190 (2014), pp. 1373–1377.

[24] J. Bauer, A. Schroer, R. Schwaiger, and Oliver Kraft. "Approaching theoretical strength in glassy carbon nanolattices". In: *Nature Materials* 15.4 (Apr. 2016), pp. 438–443. ISSN: 1476-1122. DOI: 10.1038/nmat4561. URL: http://www.nature.com/doifinder/10.1038/nmat4561%20http://www.nature.com/articles/nmat4561.

[25] D. Hull and T. W. Clyne. *An Introduction to Composite Materials*. Cambridge University Press, Aug. 1996. ISBN: 9781139170130. DOI: 10.1017/cbo9781139170130. URL: http://dx.doi.org/10.1017/CBO9781139170130.

[26] Ronald F. Gibson. *Principles of Composite Material Mechanics*. CRC Press, Feb. 2016. ISBN: 9780429190582. DOI: 10.1201/b19626. URL: http://dx.doi.org/10.1201/b19626.

[27] Michael R. Wisnom and Stephen R. Hallett. "The role of delamination in strength, failure mechanism and hole size effect in open hole tensile tests on quasi-isotropic laminates". In: *Composites Part A: Applied Science and Manufacturing* 40.4 (Apr. 2009), pp. 335–342. ISSN: 1359-835X. DOI: 10.1016/j.compositesa.2008.12.013. URL: http://dx.doi.org/10.1016/j.compositesa.2008.12.013.

[28] M. R. Wisnom. "The role of delamination in failure of fibre-reinforced composites". In: *Philosophical Transactions of the Royal Society A: Mathematical, Physical and Engineering Sciences* 370.1965 (Apr. 2012), pp. 1850–1870. ISSN: 1471-2962. DOI: 10.1098/rsta.2011.0441. URL: http://dx.doi.org/10.1098/rsta.2011.0441.

[29] David R. Clarke. "Interpenetrating Phase Composites". In: *Journal of the American Ceramic Society* 75.4 (Apr. 1992), pp. 739–758. DOI: 10.1111/j.1151-2916.1992.tb04138.x. URL: https://doi.org/10.1111/j.1151-2916.1992.tb04138.x.

[30] Jens Bauer, Martí Sala-Casanovas, Mahsa Amiri, and Lorenzo Valdevit. "Nanoarchitected metal/ceramic interpenetrating phase composites". In: *Science Advances* 8.33 (Aug. 2022). DOI: 10.1126/sciadv.abo3080. URL: https://doi.org/10.1126/sciadv.abo3080.

[31] L.D. Wegner and L.J. Gibson. "The mechanical behaviour of interpenetrating phase composites – I: modelling". In: *International Journal of Mechanical Sciences* 42.5 (May 2000), pp. 925–942. DOI: 10.1016/s0020-7403(99)00025-9. URL: https://doi.org/10.1016/s0020-7403(99)00025-9.

[32] Navya Kota, Munagala Sai Charan, Tapas Laha, and Siddhartha Roy. "Review on development of metal/ceramic interpenetrating phase composites and critical analysis of their properties". In: *Ceramics International* 48.2 (Jan. 2022), pp. 1451–1483. DOI: 10.1016/j.ceramint.2021.09.232. URL: https://doi.org/10.1016/j.ceramint.2021.09.232.

[33] D Scida. "A micromechanics model for 3D elasticity and failure of woven-fibre composite materials". In: *Composites Science and Technology* 59.4 (Mar. 1999), pp. 505–517. ISSN: 0266-3538. DOI: 10.1016/s0266-3538(98)00096-7. URL: http://dx.doi.org/10.1016/S0266-3538(98)00096-7.

[34] S. Das, K. Kandan, S. Kazemahvazi, H.N.G. Wadley, and V.S. Deshpande. "Compressive response of a 3D non-woven carbon-fibre composite". In: *International Journal of Solids and Structures* 136–137 (Apr. 2018), pp. 137–149. ISSN: 0020-7683. DOI: 10.1016/j.ijsolstr.2017.12.011. URL: http://dx.doi.org/10.1016/j.ijsolstr.2017.12.011.

[35] Yunfei Zhang, Meng-Ting Hsieh, and Lorenzo Valdevit. "Mechanical performance of 3D printed interpenetrating phase composites with spinodal topologies". In: *Composite Structures* 263 (May 2021), p. 113693. DOI: 10.1016/j.compstruct.2021.113693. URL: https://doi.org/10.1016/j.compstruct.2021.113693.

[36] Tiantian Li, Yanyu Chen, and Lifeng Wang. "Enhanced fracture toughness in architected interpenetrating phase composites by 3D printing". In: *Composites Science and Technology* 167 (Oct. 2018), pp. 251–259. DOI: 10.1016/j.compscitech.2018.08.009. URL: https://doi.org/10.1016/j.compscitech.2018.08.009.

[37] Lifeng Wang, Jacky Lau, Edwin L. Thomas, and Mary C. Boyce. "Co-Continuous Composite Materials for Stiffness, Strength, and Energy Dissipation". In: *Advanced Materials* 23.13 (Feb. 2011), pp. 1524–1529. DOI: 10.1002/adma.201003956. URL: https://doi.org/10.1002/adma.201003956.

[38] Oraib Al-Ketan, Mhd Adel Assad, and Rashid K. Abu Al-Rub. "Mechanical properties of periodic interpenetrating phase composites with novel architected microstructures". In: *Composite Structures* 176 (Sept. 2017), pp. 9–19. DOI: 10.1016/j.compstruct.2017.05.026. URL: https://doi.org/10.1016/j.compstruct.2017.05.026.

[39] J. Carlsson, A. Kuswoyo, A. Shaikeea, and N.A. Fleck. "Compression of filled, open-cell, 3D-printed Kelvin lattices". In: *Mechanics of Materials* 188 (Jan. 2024), p. 104851. ISSN: 0167-6636. DOI: 10.1016/j.mechmat.2023.104851. URL: http://dx.doi.org/10.1016/j.mechmat.2023.104851.

[40] Erdong Wang, Chao Chen, Guangzhou Zhang, Quantian Luo, Qing Li, and Guangyong Sun. "Multiaxial mechanical characterization of additively manufactured open-cell Kelvin foams". In: *Composite Structures* 305 (Feb. 2023), p. 116505. ISSN: 0263-8223. DOI: 10.1016/j.compstruct.2022.116505. URL: http://dx.doi.org/10.1016/j.compstruct.2022.116505.

[41] Vikram S. Deshpande, Norman A. Fleck, and M. F. Ashby. "Effective properties of the octet-truss lattice material". In: *Journal of the Mechanics and Physics of Solids* 49.8 (2001), pp. 1747–1769. ISSN: 00225096. DOI: 10.1016/S0022-5096(01)00010-2.

[42] *Three-Dimensional Microfabrication Using Two-photon Polymerization*. Elsevier, 2016. DOI: 10.1016/c2014-0-01016-7. URL: https://doi.org/10.1016/c2014-0-01016-7.

[43] Hao Wang et al. "Two-Photon Polymerization Lithography for Optics and Photonics: Fundamentals, Materials, Technologies, and Applications". In: *Advanced Functional Materials* (Mar. 2023), p. 2214211. DOI: 10.1002/adfm.202214211. URL: https://doi.org/10.1002/adfm.202214211.

[44] Swati Sharma, C. N. Shyam Kumar, Jan G. Korvink, and Christian Kübel. "Evolution of Glassy Carbon Microstructure: In Situ Transmission Electron Microscopy of the Pyrolysis Process". In: *Scientific Reports* 8.1 (Nov. 2018). ISSN: 2045-2322. DOI: 10.1038/s41598-018-34644-9. URL: http://dx.doi.org/10.1038/s41598-018-34644-9.

[45] W.C. Oliver and G.M. Pharr. "An improved technique for determining hardness and elastic modulus using load and displacement sensing indentation experiments". In: *Journal of Materials Research* 7.6 (June 1992), pp. 1564–1583. ISSN: 2044-5326. DOI: 10.1557/jmr.1992.1564. URL: http://dx.doi.org/10.1557/JMR.1992.1564.

[46] Yolita M. Eggeler et al. "A Review on 3D Architected Pyrolytic Carbon Produced by Additive Micro/Nanomanufacturing". In: *Advanced Functional Materials* 34.20 (June 2023). ISSN: 1616-3028. DOI: 10.1002/adfm.202302068. URL: http://dx.doi.org/10.1002/adfm.202302068.

[47] R. C. Huang and L. Anand. "Non-linear mechanical behavior of the elastomer polydimethylsiloxane (PDMS) used in the manufacture of microfluidic devices". In: 2005. URL: https://api.semanticscholar.org/CorpusID:18473213.

[48] Michael F. Ashby and David R.H. Jones. "Mechanical Properties of Polymers". In: *Engineering Materials 2*. Elsevier, 2013, pp. 419–440. ISBN: 9780080966687. DOI: 10.1016/b978-0-08-096668-7.00025-5. URL: http://dx.doi.org/10.1016/B978-0-08-096668-7.00025-5.

[49] *ASTM D695-15, Standard Test Method for Compressive Properties of Rigid Plastics*. ASTM International, West Conshohocken, PA, 2015. DOI: 10.1520/d0695-15. URL: www.astm.org.

[50] M. Danielsson, D.M. Parks, and M.C. Boyce. "Three-dimensional micromechanical modeling of voided polymeric materials". In: *Journal of the Mechanics and Physics of Solids* 50.2 (Feb. 2002), pp. 351–379. ISSN: 0022-5096. DOI: 10.1016/s0022-5096(01)00060-6. URL: http://dx.doi.org/10.1016/S0022-5096(01)00060-6.

[51] M.I. Okereke and A.I. Akpoyomare. "A virtual framework for prediction of full-field elastic response of unidirectional composites". In: *Computational Materials Science* 70 (Apr. 2013), pp. 82–99. DOI: 10.1016/j.commatsci.2012.12.036. URL: https://doi.org/10.1016/j.commatsci.2012.12.036.

[52] Wen-Yea Jang and Stelios Kyriakides. "On the crushing of aluminum open-cell foams: Part II analysis". In: *International Journal of Solids and Structures* 46.3–4 (Feb. 2009), pp. 635–650. ISSN: 0020-7683. DOI: 10.1016/j.ijsolstr.2008.10.016. URL: http://dx.doi.org/10.1016/j.ijsolstr.2008.10.016.

[53] L.L. Yan, B. Yu, B. Han, C.Q. Chen, Q.C. Zhang, and T.J. Lu. "Compressive strength and energy absorption of sandwich panels with aluminum foam-filled corrugated cores". In: *Composites Science and Technology* 86 (Sept. 2013), pp. 142–148. ISSN: 0266-3538. DOI: 10.1016/j.compscitech.2013.07.011. URL: http://dx.doi.org/10.1016/j.compscitech.2013.07.011.

[54] Bin Han, Zhi-Jia Zhang, Qian-Cheng Zhang, Qi Zhang, Tian Jian Lu, and Bing-Heng Lu. "Recent advances in hybrid lattice-cored sandwiches for enhanced multifunctional performance". In: *Extreme Mechanics Letters* 10 (Jan. 2017), pp. 58–69. ISSN: 2352-4316. DOI: 10.1016/j.eml.2016.11.009. URL: http://dx.doi.org/10.1016/j.eml.2016.11.009.

[55] Yi Ren, Yu Nie, Wei Ran, Zhuofan Liu, Lixia Wang, Chao Lou, and Wei Chen. "Mechanical Properties and Energy Absorption of Soft–Hard Dual Phase Lattice Structures Manufactured via Selective Laser Melting". In: *Metals and Materials International* 30.2 (Aug. 2023), pp. 303–314. ISSN: 2005-4149. DOI: 10.1007/s12540-023-01502-x. URL: http://dx.doi.org/10.1007/s12540-023-01502-x.

[56] Hongshuai Lei, Chuanlei Li, Jinxin Meng, Hao Zhou, Yabo Liu, Xiaoyu Zhang, Panding Wang, and Daining Fang. "Evaluation of compressive properties of SLM-fabricated multi-layer lattice structures by experimental test and -CT-based finite element analysis". In: *Materials amp; Design* 169 (May 2019), p. 107685. ISSN: 0264-1275. DOI: 10.1016/j.matdes.2019.107685. URL: http://dx.doi.org/10.1016/j.matdes.2019.107685.

[57] Youness Alvandi-Tabrizi and Afsaneh Rabiei. "Use of Composite Metal Foam for Improving Absorption of Collision Forces". In: *Procedia Materials Science* 4 (2014), pp. 377–382. ISSN: 2211-8128. DOI: 10.1016/j.mspro.2014.07.577. URL: http://dx.doi.org/10.1016/j.mspro.2014.07.577.

[58] X. Wendy Gu and Julia. R. Greer. "Ultra-strong architected Cu meso-lattices". In: *Extreme Mechanics Letters* 2 (Mar. 2015), pp. 7–14. ISSN: 2352-4316. DOI: 10.1016/j.eml.2015.01.006. URL: http://dx.doi.org/10.1016/j.eml.2015.01.006.

[59] S. Kumar, J. Ubaid, R. Abishera, A. Schiffer, and V. S. Deshpande. "Tunable Energy Absorption Characteristics of Architected Honeycombs Enabled via Additive Manufacturing". In: *ACS Applied Materials amp; Interfaces* 11.45 (Sept. 2019), pp. 42549–42560. ISSN: 1944-8252. DOI: 10.1021/acsami.9b12880. URL: http://dx.doi.org/10.1021/acsami.9b12880.

[60] Akira Kudo, Kazuya Kanamaru, Jiuhui Han, Rui Tang, Kazuaki Kisu, Takeharu Yoshii, Shin-ichi Orimo, Hirotomo Nishihara, and Mingwei Chen. "Stereolithography 3D Printed Carbon Microlattices with Hierarchical Porosity for Structural and Functional Applications". In: *Small* 19.47 (Aug. 2023). ISSN: 1613-6829. DOI: 10.1002/smll.202301525. URL: http://dx.doi.org/10.1002/smll.202301525.

[61] Ziming Ye et al. "Crack-Induced Superelastic, Strength-Tunable Carbon Nanotube Sponges". In: *Advanced Functional Materials* 33.44 (June 2023). ISSN: 1616-3028. DOI: 10.1002/adfm.202303475. URL: http://dx.doi.org/10.1002/adfm.202303475.

[62] Meng-Ting Hsieh, Chan Soo Ha, Zhenpeng Xu, Seokpum Kim, H. Felix Wu, Vlastimil Kunc, and Xiaoyu Zheng. "Stiff and strong, lightweight bi-material sandwich plate-lattices with enhanced energy absorption". In: *Journal of Materials Research* 36.18 (Aug. 2021), pp. 3628–3641. ISSN: 2044-5326. DOI: 10.1557/s43578-021-00322-2. URL: http://dx.doi.org/10.1557/s43578-021-00322-2.

[63] Gary L. Farley. *Relationship Between Mechanical-Property and Energy-Absorption Trends for Composite Tubes*. NASA Langley Technical Report Server, 1999.

[64] Minh-Son Pham, Chen Liu, Iain Todd, and Jedsada Lertthanasarn. "Damage-tolerant architected materials inspired by crystal microstructure". In: *Nature* 565.7739 (Jan. 2019), pp. 305–311. ISSN: 1476-4687. DOI: 10.1038/s41586-018-0850-3. URL: http://dx.doi.org/10.1038/s41586-018-0850-3.

[65] Chen Liu, Jedsada Lertthanasarn, and Minh-Son Pham. "The origin of the boundary strengthening in polycrystal-inspired architected materials". In: *Nature Communications* 12.1 (July 2021). ISSN: 2041-1723. DOI: 10.1038/s41467-021-24886-z. URL: http://dx.doi.org/10.1038/s41467-021-24886-z.

[66] Daniel Rayneau-Kirkhope, Silvia Bonfanti, and Stefano Zapperi. "Density scaling in the mechanics of a disordered mechanical meta-material". In: *Applied Physics Letters* 114.11 (Mar. 2019). ISSN: 1077-3118. DOI: 10.1063/1.5083027. URL: http://dx.doi.org/10.1063/1.5083027.